PTEP

Prog. Theor. Exp. Phys. **2021**, 043C01 (28 pages)
DOI: 10.1093/ptep/ptab014

Measurements of $\overline{\nu}_\mu$ and $\overline{\nu}_\mu + \nu_\mu$ charged-current cross-sections without detected pions or protons on water and hydrocarbon at a mean anti-neutrino energy of 0.86 GeV

K. Abe[1], N. Akhlaq[2], R. Akutsu[3], A. Ali[4], C. Alt[5], C. Andreopoulos[6,7], L. Anthony[8], M. Antonova[9], S. Aoki[10], A. Ariga[11], T. Arihara[12], Y. Asada[13], Y. Ashida[4], E. T. Atkin[8], Y. Awataguchi[12], S. Ban[4], M. Barbi[14], G. J. Barker[15], G. Barr[16], D. Barrow[16], C. Barry[7], M. Batkiewicz-Kwasniak[17], A. Beloshapkin[18], F. Bench[7], V. Berardi[19], S. Berkman[20,21], L. Berns[22], S. Bhadra[23], S. Bienstock[24], A. Blanchet[24], A. Blondel[24,25], S. Bolognesi[26], T. Bonus[27], B. Bourguille[28], S. B. Boyd[15], D. Brailsford[29], A. Bravar[25], D. Bravo Berguño[30], C. Bronner[1], S. Bron[25], A. Bubak[31], M. Buizza Avanzini[32], J. Calcutt[33], T. Campbell[34], S. Cao[35], S. L. Cartwright[36], M. G. Catanesi[19], A. Cervera[9], A. Chappell[15], C. Checchia[37], D. Cherdack[38], N. Chikuma[39], G. Christodoulou[40], M. Cicerchia[37,41], J. Coleman[7], G. Collazuol[37], L. Cook[3,16], D. Coplowe[16], A. Cudd[34], A. Dabrowska[17], G. De Rosa[42], T. Dealtry[29], P. F. Denner[15], S. R. Dennis[7], C. Densham[6], A. Dergacheva[18], F. Di Lodovico[43], N. Dokania[44], S. Dolan[40], T. A. Doyle[29], O. Drapier[32], J. Dumarchez[24], P. Dunne[8], A. Eguchi[39], L. Eklund[45], S. Emery-Schrenk[26], A. Ereditato[11], P. Fernandez[7], T. Feusels[20,21], A. J. Finch[29], G. A. Fiorentini[23], G. Fiorillo[42], C. Francois[11], M. Friend[35,46], Y. Fujii[35,46], R. Fujita[39], D. Fukuda[47], R. Fukuda[48], Y. Fukuda[49], K. Fusshoeller[5], K. Gameil[20,21], C. Giganti[24], T. Golan[27], M. Gonin[32], A. Gorin[18], M. Guigue[24], D. R. Hadley[15], J. T. Haigh[15], P. Hamacher-Baumann[50], D. A. Harris[23], M. Hartz[3,51], T. Hasegawa[35,46], S. Hassani[26], N. C. Hastings[35], T. Hayashino[4], Y. Hayato[1,3], A. Hiramoto[4], M. Hogan[52], J. Holeczek[31], N. T. Hong Van[53,54], T. Honjo[55], F. Iacob[37], A. K. Ichikawa[4], M. Ikeda[1], T. Ishida[35,46], T. Ishii[35,46], M. Ishitsuka[48], K. Iwamoto[39], A. Izmaylov[18], N. Izumi[48], M. Jakkapu[35], B. Jamieson[56], S. J. Jenkins[36], C. Jesús-Valls[28], M. Jiang[4], S. Johnson[34], P. Jonsson[8], C. K. Jung[44,57], P. B. Jurj[8], M. Kabirnezhad[16], A. C. Kaboth[5,58], T. Kajita[57,59], H. Kakuno[12], J. Kameda[1], D. Karlen[12,60], S. P. Kasetti[61], Y. Kataoka[1], Y. Katayama[13], T. Katori[43], Y. Kato[1], E. Kearns[3,46,62] M. Khabibullin[18], A. Khotjantsev[18], T. Kikawa[4], H. Kikutani[39], H. Kim[55], J. Kim[20,21], S. King[43], J. Kisiel[31], A. Knight[15], A. Knox[29], T. Kobata[55], T. Kobayashi[35,46], L. Koch[16], T. Koga[39,*], A. Konaka[21], L. L. Kormos[29], Y. Koshio[47,57], A. Kostin[18], K. Kowalik[63], H. Kubo[4], Y. Kudenko[18,64], N. Kukita[55], S. Kuribayashi[4], R. Kurjata[65], T. Kutter[61], M. Kuze[22], L. Labarga[30], J. Lagoda[63], M. Lamoureux[37], D. Last[66], M. Laveder[37], M. Lawe[29], M. Licciardi[32], T. Lindner[21], R. P. Litchfield[45], S. L. Liu[44], X. Li[44], A. Longhin[37], L. Ludovici[67], X. Lu[16], T. Lux[28], L. N. Machado[42], L. Magaletti[19], K. Mahn[33], M. Malek[36], S. Manly[68], L. Maret[25], A. D. Marino[34], L. Marti-Magro[1,3], J. F. Martin[51], T. Maruyama[35,46], T. Matsubara[35], K. Matsushita[39], V. Matveev[18], C. Mauger[7], K. Mavrokoridis[66], E. Mazzucato[7], M. McCarthy[26], N. McCauley[23], J. McElwee[36], K. S. McFarland[68], C. McGrew[44], A. Mefodiev[18], C. Metelko[7], M. Mezzetto[27], A. Minamino[13], O. Mineev[18], S. Mine[69], M. Miura[1,57], L. Molina Bueno[5], S. Moriyama[1,57], J. Morrison[33], Th. A. Mueller[32], L. Munteanu[26], S. Murphy[5], Y. Nagai[34], T. Nakadaira[35,46],

Funded by SCOAP[3]

M. Nakahata[1,3], Y. Nakajima[1], A. Nakamura[47], K. G. Nakamura[4], K. Nakamura[3,35,46] Y. Nakano[10], S. Nakayama[1,3], T. Nakaya[3,4], K. Nakayoshi[35,46], C. Nantais[51], C. E.R. Naseby[8], T. V. Ngoc[53], V. Q. Nguyen[24], K. Niewczas[27], K. Nishikawa[†,35], Y. Nishimura[70], E. Noah[25], T. S. Nonnenmacher[8], F. Nova[6], P. Novella[9], J. Nowak[29], J. C. Nugent[45], H. M. O'Keeffe[29], L. O'Sullivan[36], T. Odagawa[4], T. Ogawa[35], R. Okada[47], K. Okumura[3,59], T. Okusawa[55], S. M. Oser[20,21], R. A. Owen[2], Y. Oyama[35,46], V. Palladino[42], J. L. Palomino[44], V. Paolone[71], M. Pari[37], W. C. Parker[58], S. Parsa[25], J. Pasternak[8], P. Paudyal[7], M. Pavin[21], D. Payne[7], G. C. Penn[7], L. Pickering[33], C. Pidcott[36], G. Pintaudi[13], E. S. Pinzon Guerra[23], C. Pistillo[11], B. Popov[24,72], K. Porwit[31], M. Posiadala-Zezula[73], A. Pritchard[7], B. Quilain[32], T. Radermacher[50], E. Radicioni[19], B. Radics[5], P. N. Ratoff[29], E. Reinherz-Aronis[52], C. Riccio[44], E. Rondio[63], S. Roth[50], A. Rubbia[5], A. C. Ruggeri[42], C. Ruggles[45], A. Rychter[65], K. Sakashita[35,46], F. Sánchez[25], G. Santucci[23], C. M. Schloesser[5], K. Scholberg[57,74], J. Schwehr[52], M. Scott[8], Y. Seiya[55,76], T. Sekiguchi[35,46], H. Sekiya[1,3,57], D. Sgalaberna[5], R. Shah[6,16], A. Shaikhiev[18], F. Shaker[23], A. Shaykina[18], M. Shiozawa[1,3], W. Shorrock[8], A. Shvartsman[18], K. Skwarczynski[63], A. Smirnov[18], M. Smy[69], J. T. Sobczyk[27], H. Sobel[3,69], F. J.P. Soler[45], Y. Sonoda[1], R. Spina[19], J. Steinmann[50], S. Suvorov[18,24], A. Suzuki[10], S. Y. Suzuki[35,46], Y. Suzuki[3], A. A. Sztuc[8], M. Tada[35,46], M. Tajima[4], A. Takeda[1], Y. Takeuchi[3,10], H. K. Tanaka[1,57], H. A. Tanaka[51,75], S. Tanaka[55], Y. Tanihara[13], M. Tani[4], N. Teshima[55], L. F. Thompson[36], W. Toki[52], C. Touramanis[7], T. Towstego[51], K. M. Tsui[7], T. Tsukamoto[35,46], M. Tzanov[61], Y. Uchida[8], W. Uno[4], M. Vagins[3,69], S. Valder[15], Z. Vallari[44], D. Vargas[28], G. Vasseur[26], C. Vilela[40], W. G.S. Vinning[15], T. Vladisavljevic[6], V. V. Volkov[18], T. Wachala[17], J. Walker[56], J. G. Walsh[29], Y. Wang[44], D. Wark[6,16], M. O. Wascko[8], A. Weber[6,16], R. Wendell[4,57], M. J. Wilking[44], C. Wilkinson[11], J. R. Wilson[43], R. J. Wilson[52], K. Wood[44], C. Wret[68], J. Xia[59], Y. Yamada[26,35], K. Yamamoto[55,76], C. Yanagisawa[44,77], G. Yang[44], T. Yano[1], K. Yasutome[4], S. Yen[21], N. Yershov[18], M. Yokoyama[39,57], T. Yoshida[22], Y. Yoshimoto[39], M. Yu[23], A. Zalewska[17], J. Zalipska[63], K. Zaremba[65], G. Zarnecki[63], M. Ziembicki[65], E. D. Zimmerman[34], M. Zito[24], S. Zsoldos[43], and A. Zykova[18]

[1]*University of Tokyo, Institute for Cosmic Ray Research, Kamioka Observatory, Kamioka, Japan*
[2]*Queen Mary University of London, School of Physics and Astronomy, London, United Kingdom*
[3]*Kavli Institute for the Physics and Mathematics of the Universe (WPI), The University of Tokyo Institutes for Advanced Study, University of Tokyo, Kashiwa, Chiba, Japan*
[4]*Kyoto University, Department of Physics, Kyoto, Japan*
[5]*ETH Zurich, Institute for Particle Physics and Astrophysics, Zurich, Switzerland*
[6]*STFC, Rutherford Appleton Laboratory, Harwell Oxford, and Daresbury Laboratory, Warrington, United Kingdom*
[7]*University of Liverpool, Department of Physics, Liverpool, United Kingdom*
[8]*Imperial College London, Department of Physics, London, United Kingdom*
[9]*IFIC (CSIC & University of Valencia), Valencia, Spain*
[10]*Kobe University, Kobe, Japan*
[11]*University of Bern, Albert Einstein Center for Fundamental Physics, Laboratory for High Energy Physics (LHEP), Bern, Switzerland*
[12]*Tokyo Metropolitan University, Department of Physics, Tokyo, Japan*
[13]*Yokohama National University, Faculty of Engineering, Yokohama, Japan*
[14]*University of Regina, Department of Physics, Regina, Saskatchewan, Canada*
[15]*University of Warwick, Department of Physics, Coventry, United Kingdom*
[16]*Oxford University, Department of Physics, Oxford, United Kingdom*
[17]*H. Niewodniczanski Institute of Nuclear Physics PAN, Cracow, Poland*
[18]*Institute for Nuclear Research of the Russian Academy of Sciences, Moscow, Russia*
[19]*INFN Sezione di Bari and Università e Politecnico di Bari, Dipartimento Interuniversitario di Fisica, Bari, Italy*
[20]*University of British Columbia, Department of Physics and Astronomy, Vancouver, British Columbia, Canada*

[21]*TRIUMF, Vancouver, British Columbia, Canada*
[22]*Tokyo Institute of Technology, Department of Physics, Tokyo, Japan*
[23]*York University, Department of Physics and Astronomy, Toronto, Ontario, Canada*
[24]*Sorbonne Université, Université Paris Diderot, CNRS/IN2P3, Laboratoire de Physique Nucléaire et de Hautes Energies (LPNHE), Paris, France*
[25]*University of Geneva, Section de Physique, DPNC, Geneva, Switzerland*
[26]*IRFU, CEA, Université Paris-Saclay, F-91191 Gif-sur-Yvette, France*
[27]*Wroclaw University, Faculty of Physics and Astronomy, Wroclaw, Poland*
[28]*Institut de Fisica d'Altes Energies (IFAE) - The Barcelona Institute of Science and Technology, Campus UAB, Bellaterra (Barcelona) Spain*
[29]*Lancaster University, Physics Department, Lancaster, United Kingdom*
[30]*University Autonoma Madrid, Department of Theoretical Physics, 28049 Madrid, Spain*
[31]*University of Silesia, Institute of Physics, Katowice, Poland*
[32]*Ecole Polytechnique, IN2P3-CNRS, Laboratoire Leprince-Ringuet, Palaiseau, France*
[33]*Michigan State University, Department of Physics and Astronomy, East Lansing, Michigan, U.S.A.*
[34]*University of Colorado at Boulder, Department of Physics, Boulder, Colorado, U.S.A.*
[35]*High Energy Accelerator Research Organization (KEK), Tsukuba, Ibaraki, Japan*
[36]*University of Sheffield, Department of Physics and Astronomy, Sheffield, United Kingdom*
[37]*INFN Sezione di Padova and Università di Padova, Dipartimento di Fisica, Padova, Italy*
[38]*University of Houston, Department of Physics, Houston, Texas, U.S.A.*
[39]*University of Tokyo, Department of Physics, Tokyo, Japan*
[40]*CERN European Organization for Nuclear Research, CH-1211 GenÃ¨ve 23, Switzerland*
[41]*INFN-Laboratori Nazionali di Legnaro*
[42]*INFN Sezione di Napoli and Università di Napoli, Dipartimento di Fisica, Napoli, Italy*
[43]*King's College London, Department of Physics, Strand, London WC2R 2LS, United Kingdom*
[44]*State University of New York at Stony Brook, Department of Physics and Astronomy, Stony Brook, New York, U.S.A.*
[45]*University of Glasgow, School of Physics and Astronomy, Glasgow, United Kingdom*
[46]*J-PARC, Tokai, Japan*
[47]*Okayama University, Department of Physics, Okayama, Japan*
[48]*Tokyo University of Science, Faculty of Science and Technology, Department of Physics, Noda, Chiba, Japan*
[49]*Miyagi University of Education, Department of Physics, Sendai, Japan*
[50]*RWTH Aachen University, III. Physikalisches Institut, Aachen, Germany*
[51]*University of Toronto, Department of Physics, Toronto, Ontario, Canada*
[52]*Colorado State University, Department of Physics, Fort Collins, Colorado, U.S.A.*
[53]*Institute For Interdisciplinary Research in Science and Education (IFIRSE), ICISE, Quy Nhon, Vietnam*
[54]*International Centre of Physics, Institute of Physics (IOP), Vietnam Academy of Science and Technology (VAST), 10 Dao Tan, Ba Dinh, Hanoi, Vietnam*
[55]*Osaka City University, Department of Physics, Osaka, Japan*
[56]*University of Winnipeg, Department of Physics, Winnipeg, Manitoba, Canada*
[57]*Affiliated member at Kavli IPMU (WPI), the University of Tokyo, Japan*
[58]*Royal Holloway University of London, Department of Physics, Egham, Surrey, United Kingdom*
[59]*University of Tokyo, Institute for Cosmic Ray Research, Research Center for Cosmic Neutrinos, Kashiwa, Japan*
[60]*University of Victoria, Department of Physics and Astronomy, Victoria, British Columbia, Canada*
[61]*Louisiana State University, Department of Physics and Astronomy, Baton Rouge, Louisiana, U.S.A.*
[62]*Boston University, Department of Physics, Boston, Massachusetts, U.S.A.*
[63]*National Centre for Nuclear Research, Warsaw, Poland*
[64]*National Research Nuclear University "MEPhI" and Moscow Institute of Physics and Technology, Moscow, Russia*
[65]*Warsaw University of Technology, Institute of Radioelectronics and Multimedia Technology, Warsaw, Poland*
[66]*University of Pennsylvania, Department of Physics and Astronomy, Philadelphia, PA, 19104, USA.*
[67]*INFN Sezione di Roma and Università di Roma "La Sapienza", Roma, Italy*

[68] *University of Rochester, Department of Physics and Astronomy, Rochester, New York, U.S.A.*
[69] *University of California, Irvine, Department of Physics and Astronomy, Irvine, California, U.S.A.*
[70] *Keio University, Department of Physics, Kanagawa, Japan*
[71] *University of Pittsburgh, Department of Physics and Astronomy, Pittsburgh, Pennsylvania, U.S.A.*
[72] *JINR, Dubna, Russia*
[73] *University of Warsaw, Faculty of Physics, Warsaw, Poland*
[74] *Duke University, Department of Physics, Durham, North Carolina, U.S.A.*
[75] *SLAC National Accelerator Laboratory, Stanford University, Menlo Park, California, USA*
[76] *Nambu Yoichiro Institute of Theoretical and Experimental Physics (NITEP)*
[77] *BMCC/CUNY, Science Department, New York, New York, U.S.A.*
*E-mail: taichiro@post.kek.jp
†Deceased.
Received May 15, 2020; Revised January 26, 2021; Accepted January 26, 2021; Published March 2, 2021

We report measurements of the flux-integrated $\overline{\nu}_\mu$ and $\overline{\nu}_\mu + \nu_\mu$ charged-current cross-sections on water and hydrocarbon targets using the T2K anti-neutrino beam with a mean beam energy of 0.86 GeV. The signal is defined as the (anti-)neutrino charged-current interaction with one induced $\mu^\pm$ and no detected charged pion or proton. These measurements are performed using a new WAGASCI module recently added to the T2K setup in combination with the INGRID Proton Module. The phase space of muons is restricted to the high-detection efficiency region, $p_\mu > 400$ MeV/c and $\theta_\mu < 30°$, in the laboratory frame. An absence of pions and protons in the detectable phase spaces of $p_\pi > 200$ MeV/c, $\theta_\pi < 70°$ and $p_\mathrm{p} > 600$ MeV/c, $\theta_\mathrm{p} < 70°$ is required. In this paper, both the $\overline{\nu}_\mu$ cross-sections and $\overline{\nu}_\mu + \nu_\mu$ cross-sections on water and hydrocarbon targets and their ratios are provided by using the D'Agostini unfolding method. The results of the integrated $\overline{\nu}_\mu$ cross-section measurements over this phase space are $\sigma_{\mathrm{H_2O}} = (1.082 \pm 0.068(\mathrm{stat.})^{+0.145}_{-0.128}(\mathrm{syst.})) \times 10^{-39}\,\mathrm{cm}^2/\mathrm{nucleon}$, $\sigma_{\mathrm{CH}} = (1.096 \pm 0.054(\mathrm{stat.})^{+0.132}_{-0.117}(\mathrm{syst.})) \times 10^{-39}\,\mathrm{cm}^2/\mathrm{nucleon}$, and $\sigma_{\mathrm{H_2O}}/\sigma_{\mathrm{CH}} = 0.987 \pm 0.078(\mathrm{stat.})^{+0.093}_{-0.090}(\mathrm{syst.})$. The $\overline{\nu}_\mu + \nu_\mu$ cross-section is $\sigma_{\mathrm{H_2O}} = (1.155 \pm 0.064(\mathrm{stat.})^{+0.148}_{-0.129}(\mathrm{syst.})) \times 10^{-39}\,\mathrm{cm}^2/\mathrm{nucleon}$, $\sigma_{\mathrm{CH}} = (1.159 \pm 0.049(\mathrm{stat.})^{+0.129}_{-0.115}(\mathrm{syst.})) \times 10^{-39}\,\mathrm{cm}^2/\mathrm{nucleon}$, and $\sigma_{\mathrm{H_2O}}/\sigma_{\mathrm{CH}} = 0.996 \pm 0.069(\mathrm{stat.})^{+0.083}_{-0.078}(\mathrm{syst.})$.

Subject Index C04, C32

1. Introduction

The Tokai-to-Kamioka (T2K) experiment [1] is a long-baseline neutrino oscillation experiment in Japan. Using either the ν_μ or the $\overline{\nu}_\mu$ beam produced at the J-PARC accelerator complex, both electron (anti-)neutrino appearance and muon (anti-)neutrino disappearance are measured at the far detector, Super-Kamiokande (SK). T2K aims to make precision measurements of neutrino oscillation parameters, including a search for *CP* violation in the leptonic sector by precisely measuring the (anti-)neutrino oscillation. In these measurements, the neutrino event rate at SK is constrained by the cross-section and neutrino flux measured in the near detector, ND280. The ND280 includes two fine-grained detectors, FGD1 and FGD2 [2], used as a target for neutrino interactions and as a tracking device. The FGD1 interaction target is made up of plastic scintillators, and FGD2 consists of water and plastic scintillator targets, while SK is a water-target detector. Uncertainties in the modeling of neutrino–nucleus interactions due to the difference in the target at the near and far detectors constitute an additional source of systematic uncertainties in the T2K oscillation analysis. In addition, poorly understood nuclear effects like the so-called two-particle–two-hole (2p2h) process with large uncertainties motivate testing the interaction model at multiple neutrino energies. The neutrino-interaction model is used to extrapolate the neutrino event distributions from the near-detector measurements to the far detector as well as outgoing particle kinematics. First,

the neutrino energy distribution at the far detector is different from that at the near detector mainly because of neutrino oscillations. Furthermore, the T2K off-axis near-detector angular acceptance for charged particles is more limited than that of the far detector. Moreover, the near-detector event rate also includes significant interactions on materials other than the far-detector target. The interaction model is tuned from the near-detector measurement and its parameterization can be incomplete. Therefore, testing the interaction model with different target materials and at various ranges of neutrino energies is essential to improve the T2K oscillation analysis.

In the T2K experiment, the neutrino beam is directed 2.5 degrees off-axis with respect to the SK direction to ensure that the detector sees a narrow-band neutrino beam with a peak energy at 0.6 GeV, which maximizes the oscillation probability. In this energy range, neutrino interactions with nucleons are dominated by charged-current quasi-elastic (CCQE) and charged-current resonant-pion production (CC-resonant). The neutrino energies from incoming CCQE interactions are reconstructed from the outgoing charged lepton kinematics. The neutrino energies of the CCQE candidate events are reconstructed from the outgoing charged lepton kinematics assuming the kinematics of the CCQE interaction. As a consequence, if multi-nucleon interactions or pion absorption occur in the nucleus, 2p2h and CC-resonant interactions may be misidentified as CCQE interactions because only a muon-like track may be observed in the final state. Furthermore, the reconstructed neutrino energy spectrum could be distorted. For this reason, in modern experiments, signals are classified by final-state particles, such as protons and pions. For example, CC0π (charged-current interactions with no pions in the final state) cross-sections are measured instead of measuring CCQE cross-sections making them less dependent on nuclear models.

So far, T2K has published two results of neutrino cross-sections on water at a mean neutrino energy of 0.6 GeV: a CC-resonant π^+ production cross-section using FGD2 [3] and a CC0π cross-section using a dedicated water target in the ND280 detector, called the PØD [4]. CC-inclusive neutrino cross-sections using the INGRID Water Module, which consists of 80% water and 20% plastic scintillators, with a mean neutrino energy of 1.5 GeV [5] have also been measured. However, there has been only one publication of CC0π anti-neutrino cross-sections on water using PØD [6] with a neutrino energy peak at 0.6 GeV. In this article, we measure CC0π 0p (CC0π without detected protons) cross-sections on water and hydrocarbon in anti-neutrino beam mode by using a new neutrino detector called the WAGASCI module [7] and other T2K detectors, the Proton Module [8], and the INGRID module [9] with a mean neutrino energy of 0.86 GeV at an off-axis angle of 1.5 degrees. As described in Sect. 2.2, the WAGASCI module and the INGRID Water Module are basically the same except for the detector position and electronics. In the future, we will use both detectors to measure neutrino cross-sections at an off-axis angle of 1.5 degrees.

Hereafter, we will describe the experimental apparatus, the Monte Carlo simulations, the datasets, the event selections, the analysis method, the systematic uncertainties, and the results.

2. Experimental apparatus

2.1. Neutrino beam

The accelerator complex J-PARC in Tokai (Japan) is composed of a linear accelerator (LINAC), a rapid cycling synchrotron (RCS), and the main ring (MR). The 30 GeV proton beam is extracted from the MR every 2.48 s. The beam spill consists of eight bunches with 581 ns interval. The protons impinge onto a graphite target fixed in the most upstream electromagnetic horn. The charged hadrons produced are focused by three electromagnetic horns into a 96 m-long decay volume where they produce ν_μ ($\overline{\nu}_\mu$) and μ^+ (μ^-). By changing the polarity of the horns, the beam mode can be

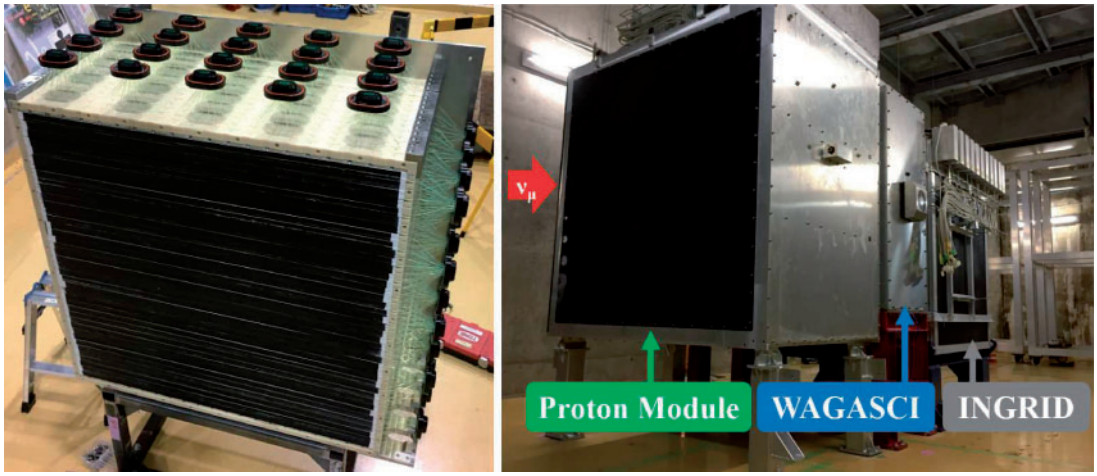

Fig. 1. The WAGASCI module before installation into the water tank (left). Detectors installed at the J-PARC neutrino-monitor building (right).

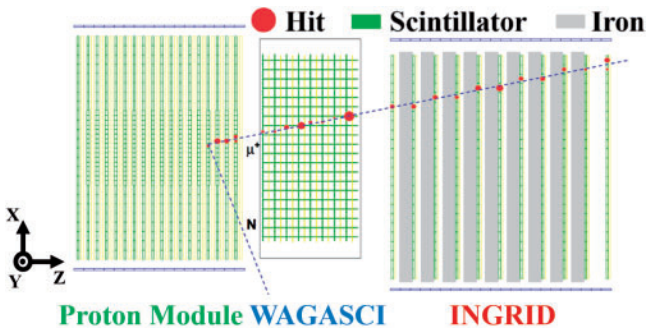

Fig. 2. Typical neutrino event display for a simulated neutrino event in the Proton Module. The beam axis corresponds to the z-axis. The muon angle is defined as the scattering angle with respect to the z-axis.

switched between the neutrino and anti-neutrino modes. In this article, the data are collected in the anti-neutrino mode with a beam power of about 470 kW.

2.2. Detector configuration

We use two detectors with different interaction targets, the WAGASCI module (water) and the Proton Module (hydrocarbon). The INGRID module is located at the most downstream position as shown in Fig. 1, and is used as a muon detector. These detectors have been located at an off-axis angle of 1.5 degrees in the T2K near-detector hall since August 2017. They are exposed to neutrinos with a higher energy distribution than the ND280 detector, since the off-axis angle is smaller than the ND280 angle of 2.5 degrees. A typical event display is shown in Fig. 2.

The WAGASCI module is a neutrino detector with 0.6 tons of water and 1280 plastic scintillator bars. The total volume fraction of water target in the fiducial volume is 80%, a larger fraction than in other T2K detectors (PØD and FGD2) [2]. The type of scintillator bar ($3 \times 25 \times 1020$ mm^3) and wavelength-shifting (WLS) fiber (Kuraray, Y-11(200)) used in the WAGASCI module is the same as that used in the INGRID Water Module [5]. The readout electronics are newly developed with a silicon PM integrated read-out chip (SPIROC), which is a 36-channel auto-triggered front-end ASIC. The WAGASCI module consists of 16 scintillator tracking planes in total, and each tracking plane consists of 40 scintillators positioned perpendicularly to the neutrino-beam axis (plane scintillator)

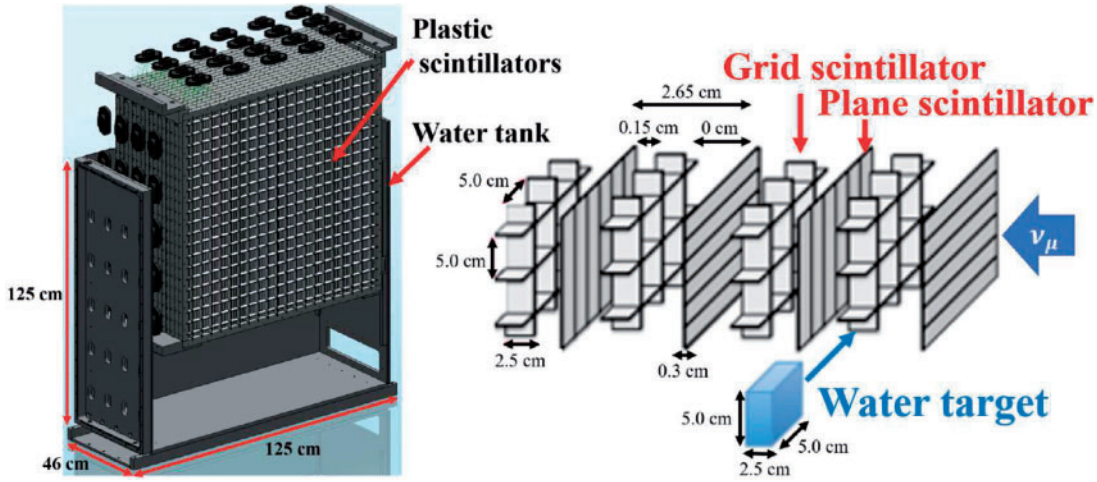

Fig. 3. Schematic view of the WAGASCI module (left) and its scintillator structure (right).

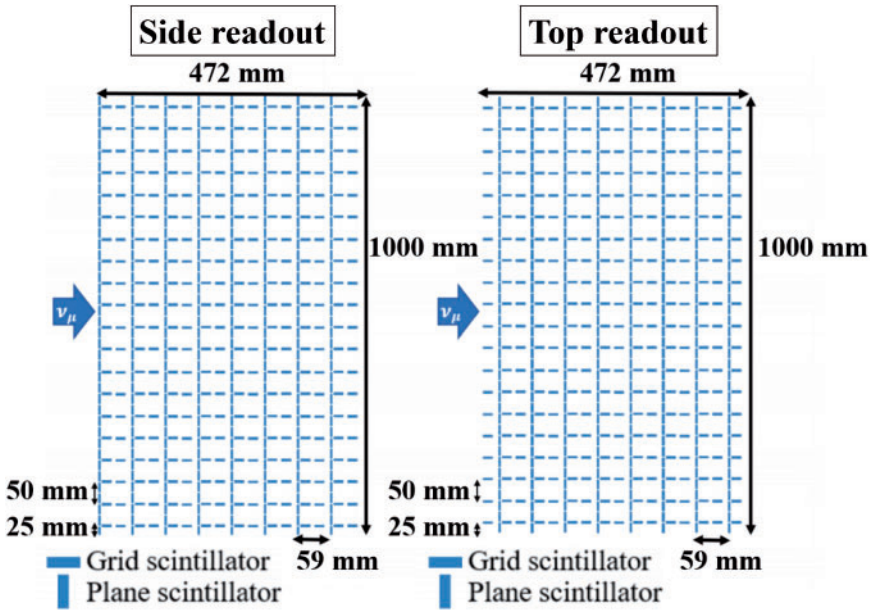

Fig. 4. Scintillators of the WAGASCI module. Their signals are read out by MPPCs implemented in the side (left) and top (right) of the WAGASCI module.

and another 40 scintillators positioned in parallel to the beam with a grid structure (grid scintillator), as shown in Fig. 3. Figure 4 shows a schematic view of the scintillators from the x- and y-directions, where the definition of the coordinate system is shown in Fig. 2.

The Proton Module is a fully active tracking detector. It consists of 34 tracking planes, where each tracking plane is an array of two types of 32 scintillator bars, as shown in Fig. 5. Two types of scintillators, SciBar type ($13 \times 25 \times 1203$ mm^3) and INGRID type ($10 \times 50 \times 1203$ mm^3), are used, and their chemical composition is the same as that of the WAGASCI-type scintillator bar. The six veto planes surrounding the tracking planes are used to track the charged particles coming from outside the Proton Module. The tracking planes also serve as the neutrino-interaction target. The

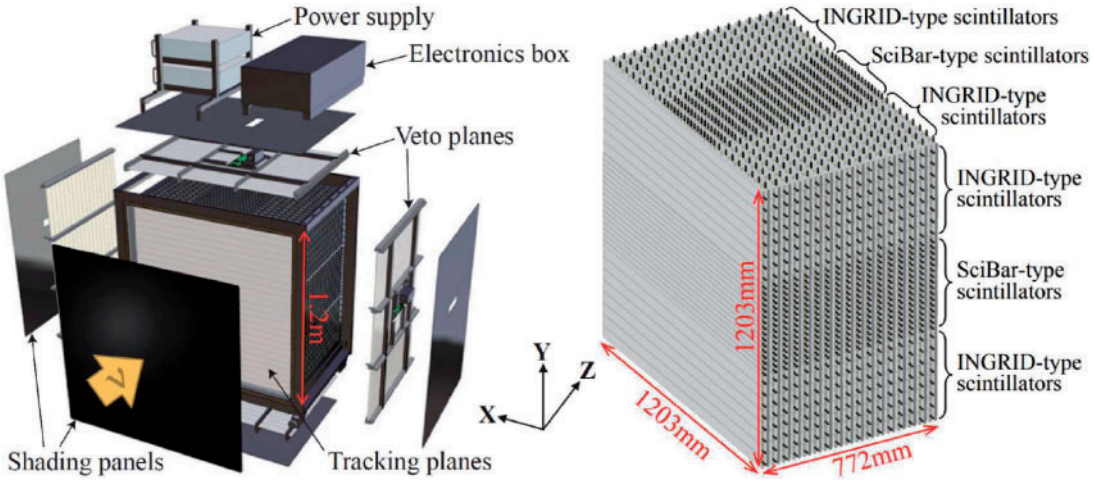

Fig. 5. Schematic view of the Proton Module (left) and its scintillator structure (right).

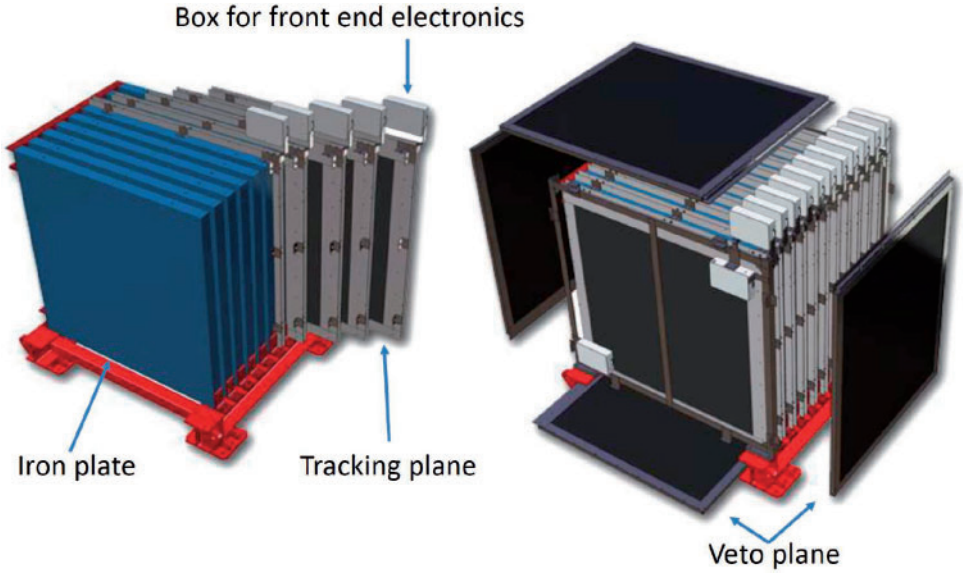

Fig. 6. Schematic view of the INGRID module.

target mass in the fiducial volume is 303 kg in total, which corresponds to 98% of the total target mass. More detailed information about the Proton Module can be found in Ref. [8].

The INGRID module has a sandwich structure comprising nine iron plates and eleven tracking planes that are surrounded by veto planes, as shown in Fig. 6. The tracking planes are formed by two scintillator layers each of which is composed of 24 scintillator bars oriented perpendicularly to one another. The thicknesses of each iron plate and scintillator bar are 6.5 cm and 1.0 cm, respectively. More detailed information about the INGRID module can be found in Ref. [9].

In all three detectors, the scintillation light emitted from the scintillator bar is collected by a WLS fiber, and it is detected by a multi-pixel photon counter (MPPC) [10]. To digitize and record the integrated charge and hit timing of 1280 channels, SPIROC2D electronics [11] are used for the WAGASCI module, and Trip-t electronics [12] are used for the Proton Module and the INGRID

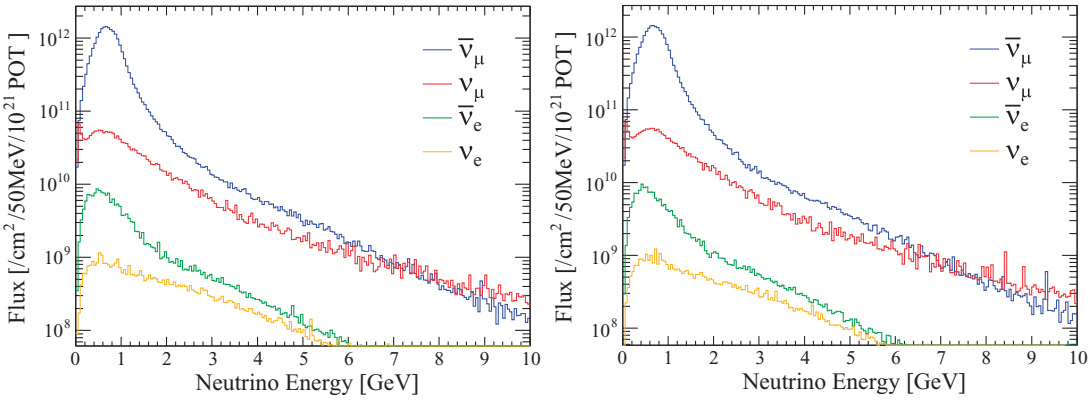

Fig. 7. Predicted (anti-)neutrino fluxes at the WAGASCI module (left) and the Proton Module (right).

Table 1. Flux-integrated $\overline{\nu}_\mu$ CC0π0p cross-sections per nucleon on H_2O and CH predicted by NEUT.

Cross-section	NEUT expectation with RPA	NEUT expectation without RPA
σ_{H_2O}	1.013×10^{-39} cm^2	1.189×10^{-39} cm^2
σ_{CH}	1.051×10^{-39} cm^2	1.278×10^{-39} cm^2
$\sigma_{H_2O}/\sigma_{CH}$	0.964	0.930

module. For each beam bunch, the threshold is set to 2.5 p.e. (photon equivalent) to exclude accidental dark noise from the MPPCs.

3. Monte Carlo simulation

To estimate backgrounds, neutrino fluxes, and signal detection efficiencies, a set of Monte Carlo (MC) simulations is used as follows:

- JNUBEAM [13] (version 13a) for neutrino fluxes,
- NEUT [14] (version 5.3.3) for neutrino interactions with nuclei,
- GEANT4 [15] (v9r2p01n00)-based software for the transport and detection of secondary particles.

Software settings for the simulation are the same as those used in Ref. [5]. The anti-neutrino beam energy spectra at the WAGASCI and Proton Module positions predicted by JNUBEAM, with hadronic processes tuned from the NA61/SHINE measurements [16], are shown in Fig. 7. The mean neutrino energy is 0.86 GeV, and the peak is at 0.66 GeV with 1σ spread of $^{+0.40}_{-0.25}$ GeV. The flux-integrated CC cross-sections per nucleon predicted by NEUT are summarized in Table 1. To compare predicted neutrino cross-sections in Sect. 7, an alternative event generator, GENIE [17] (version 2.12.8), is also used. In both generators, a relativistic Fermi gas (RFG) model [18] is used, but the Bodek–Ritchie modifications [19,20] are implemented in GENIE. The parameters used in the RFG calculations (M_A, p_f, E_b) are different between the two generators. The most significant difference concerns the axial mass where $M_A^{QE} = 1.15$ GeV and $M_A^{Res} = 0.95$ GeV for NEUT, and $M_A^{QE} = 0.99$ GeV and $M_A^{Res} = 1.12$ GeV for GENIE. In NEUT, the random-phase approximation (RPA) [21] and multi-nucleon (2p2h) interactions [22] are considered. In addition, they both use the Rein–Sehgal model [23,24] for single-meson production, the Berger–Sehgal model [25] for coherent-pion production, and Glück–Reya–Vogt-1998 (GRV98) [26] parton distributions with

Bodek–Yang modifications [27,28] for deep inelastic scattering. NEUT is also used for the T2K neutrino oscillation analysis, and more details can be found in Ref. [29].

4. Datasets and event selections

In this article, data collected from October 2017 to May 2018 are used. The datasets include statistics of 7.91×10^{20} protons on target (POT) in the anti-neutrino mode. The signal events in the WAGASCI module and the Proton Module are selected from these data. In this analysis, the signal is defined as the charged-current interaction with no detected pions or protons. This signal is characterized by a muon-like track produced inside the detector. The cross-section is calculated for signal events both from $\overline{\nu}_\mu$ interactions ($\overline{\nu}_\mu$ cross-section) and $\overline{\nu}_\mu + \nu_\mu$ interactions ($\overline{\nu}_\mu + \nu_\mu$ cross-section), as described in Sect. 5.2.

The selections applied to the two detectors are similar to those in a previous analysis [5], where cross-sections on water and hydrocarbon targets were measured. The selection criteria in this analysis are briefly described below.

4.1. Selections for the WAGASCI module

A scintillator channel having an ADC charge greater than 2.5 p.e. is defined as a "hit". Based on a cellular automaton algorithm [30], these hits are fitted by a line (track reconstruction). The 2D tracks are reconstructed in each detector from more than two hits in a beam bunch, and then at least one track in the WAGASCI module is required to be matched with a reconstructed track in the INGRID module to select a muon-like track. 3D tracks are searched for among pairs of 2D *XZ* tracks and *YZ* tracks. After the reconstruction of the 3D tracks, the upstream point of the longest track is defined as a neutrino-interaction vertex.

Subsequently, in order to reduce non-beam backgrounds such as cosmic rays, the event timing for a vertex is required to be within 100 ns from the expected beam-bunch timing (beam-timing cut). In addition, to reduce the beam-induced backgrounds mainly from neutrino interactions in the walls of the detector hall, two cuts are applied. First, if the most upstream point of a reconstructed track is in the first or second plane of the parallel scintillators, then that event is excluded. Second, if a vertex is outside the fiducial volume (FV), then that event is excluded. The FV is defined as the central area of the WAGASCI module with dimensions of 70 cm (in the x-coordinate) $\times$ 70 cm (in the y-coordinate) $\times$ 21 cm (in the z-coordinate).

Since the WAGASCI module lies closer to the INGRID module, its angular acceptance for INGRID-matched tracks is larger than the Proton Module's. In order to obtain a similar angular acceptance to that of the Proton Module, an extrapolation of the reconstructed track from the WAGASCI module is required to reach an imaginary INGRID module. The imaginary INGRID module is set as shown in Fig. 8 so that the distance between the downstream edge of the Proton Module and the upstream edge of the INGRID module (1034.5 cm) is almost the same as that between the downstream edge of the WAGASCI module and the upstream edge of the imaginary INGRID module (1035.5 cm). This cut is called "additional acceptance" selection.

For signal interactions, a single muon-like track is expected in the final state. To reduce the multi-track backgrounds from other neutrino interactions, events with more than one track are excluded.

The number of selected events and the background fraction in the WAGASCI module are summarized in Table 2. The last cut of the reconstructed track angle is due to the final selection acceptance, and it is described in Sect. 4.3. The neutrino energy, muon momentum, and angular distributions of the selected events predicted by the MC simulation are shown in Fig. 9. The left panel of Fig. 10

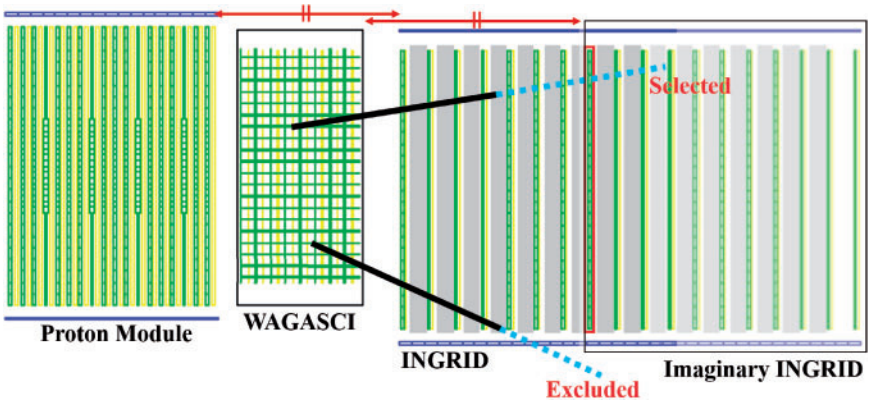

Fig. 8. Schematic view of selected and excluded events by the angular acceptance cut for the WAGASCI module. If the extrapolated track from the WAGASCI module reaches the imaginary INGRID module, the event is selected.

Table 2. Summary of event selections for the WAGASCI module. The numbers in brackets represent the fraction of the total number of events passing each selection. The number of events predicted by MC is normalized to the actual recorded POT (7.9×10^{20}).

Selection	MC					Data	Data/MC
	$\overline{\nu}_\mu$	ν_μ	$\nu_e + \overline{\nu}_e$	External BG	Total		
Event reconstruction	5559.1 (29.4%)	2597.9 (13.8%)	149.9 (0.8%)	10 582.9 (56.0%)	18 889.7 (100.0%)	20 728	1.10
Beam timing	5485.5 (29.6%)	2462.8 (13.3%)	142.3 (0.8%)	10 439.1 (56.3%)	18 529.7 (100.0%)	20 095	1.08
Upstream veto	3925.3 (33.1%)	1755.0 (14.8%)	83.0 (0.7%)	6081.8 (51.3%)	11 845.1 (100.0%)	12 236	1.03
Fiducial volume	1936.9 (66.8%)	812.8 (28.0%)	38.7 (1.3%)	112.3 (3.9%)	2900.7 (100.0%)	2797	0.96
Additional acceptance	1279.9 (67.8%)	497.4 (26.4%)	28.3 (1.5%)	81.5 (4.3%)	1887.1 (100.0%)	1783	0.94
One-track extraction	1075.7 (77.2%)	224.5 (16.1%)	17.3 (1.2%)	76.5 (5.5%)	1394.0 (100.0%)	1406	1.01
Reconstructed track angle	969.5 (76.8%)	203.5 (16.1%)	16.5 (1.3%)	72.3 (5.7%)	1261.9 (100.0%)	1279	1.01

shows the angular distribution of the reconstructed single muon-like track for events passing the one-track extraction in the WAGASCI module.

4.2. Selections for the Proton Module

Selection criteria for the Proton Module basically use the same method as those for the WAGASCI module, except for the 2D track matching. Since the WAGASCI module is located between the Proton Module and the INGRID module, 2D tracks in the Proton Module are required to be matched to both the WAGASCI module and the INGRID module.

The number of selected events and the background fraction in the Proton Module are summarized in Table 3. The neutrino energy, muon momentum, and angular distributions of the selected events predicted by the MC simulation are shown in Fig. 11. The right panel of Fig. 10 shows the angular

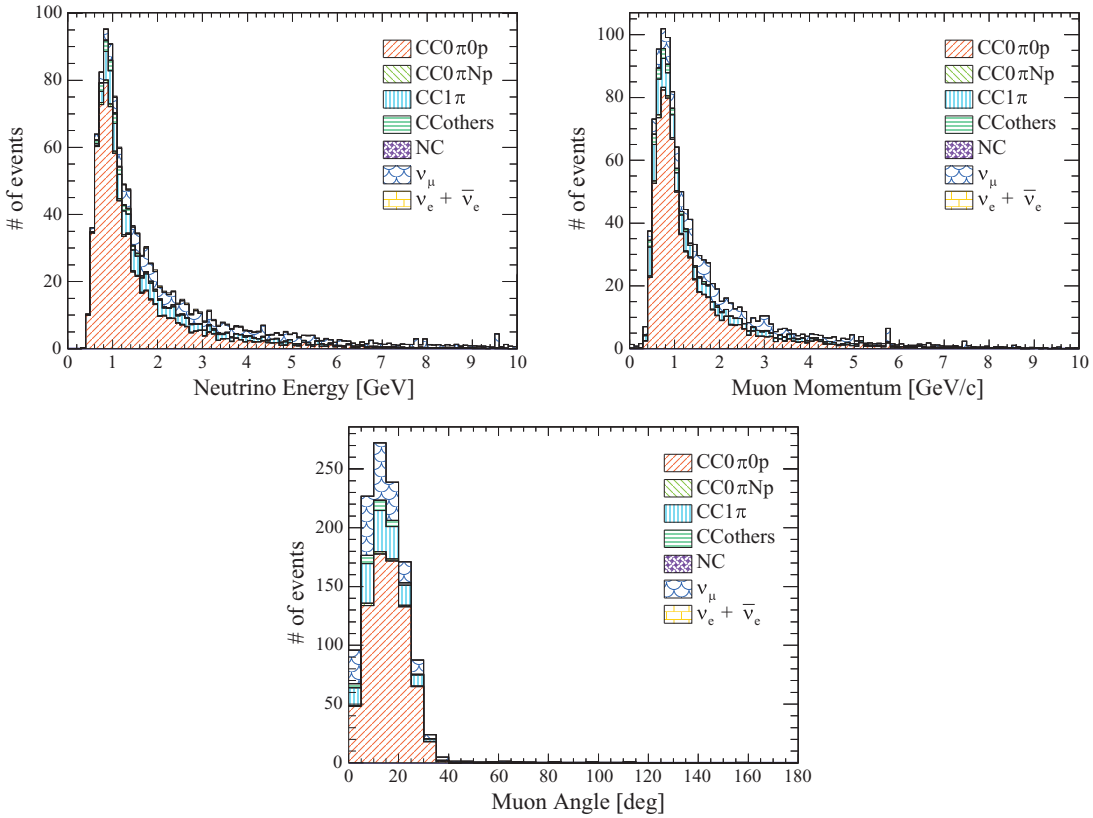

Fig. 9. Simulated true distribution of the selected events in the WAGASCI module as a function of neutrino energy (top left), muon momentum (top right), and muon angle (bottom).

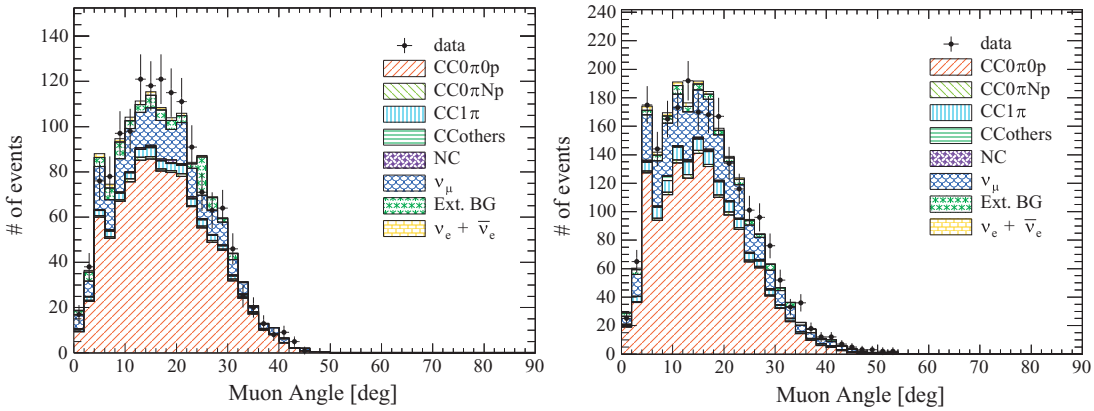

Fig. 10. Angular distributions of the longest reconstructed track matched with the INGRID track after one-track extraction for the WAGASCI module (left) and the Proton Module (right).

distribution of the reconstructed single muon-like track for events passing the one-track extraction in the Proton Module.

4.3. Selection efficiencies

Figure 12 shows selection efficiencies of CC events for the WAGASCI module and the Proton Module as a function of true muon scattering angle and momentum. The phase spaces of induced muons are restricted to the high-detection-efficiency region, $\theta_\mu < 30°$ and $p_\mu > 400$ MeV/c, in

Table 3. Summary of event selections for the Proton Module. The numbers in brackets represent the fraction of the total number of events passing each selection. The number of events predicted by MC is normalized to the actual recorded POT (7.9×10^{20}).

Selection	MC					Data	Data/MC
	$\overline{\nu}_\mu$	ν_μ	$\nu_e + \overline{\nu}_e$	External BG	Total		
Event reconstruction	4813.4 (2.4%)	2219.1 (1.1%)	104.1 (0.1%)	195 761.9 (96.5%)	202 898.5 (100.0%)	191 554	0.94
Beam timing	4807.8 (2.4%)	2201.8 (1.1%)	103.3 (0.1%)	195 691.1 (96.5%)	202 804.0 (100.0%)	191 118	0.94
Upstream veto	4223.2 (11.3%)	1883.3 (5.0%)	88.6 (0.2%)	31 118.6 (83.4%)	37 313.7 (100.0%)	40 593	1.09
Fiducial volume	1865.8 (67.4%)	792.0 (28.6%)	39.0 (1.4%)	71.3 (2.6%)	2768.2 (100.0%)	2623	0.95
Additional acceptance	1865.8 (67.4%)	792.0 (28.6%)	39.0 (1.4%)	71.3 (2.6%)	2768.2 (100.0%)	2623	0.95
One-track extraction	1620.6 (75.6%)	429.0 (20.0%)	25.0 (1.2%)	68.5 (3.2%)	2143.1 (100.0%)	2152	1.00
Reconstructed track angle	1514.5 (76.4%)	390.1 (19.7%)	23.7 (1.2%)	54.8 (2.8%)	1983.1 (100.0%)	1967	0.99

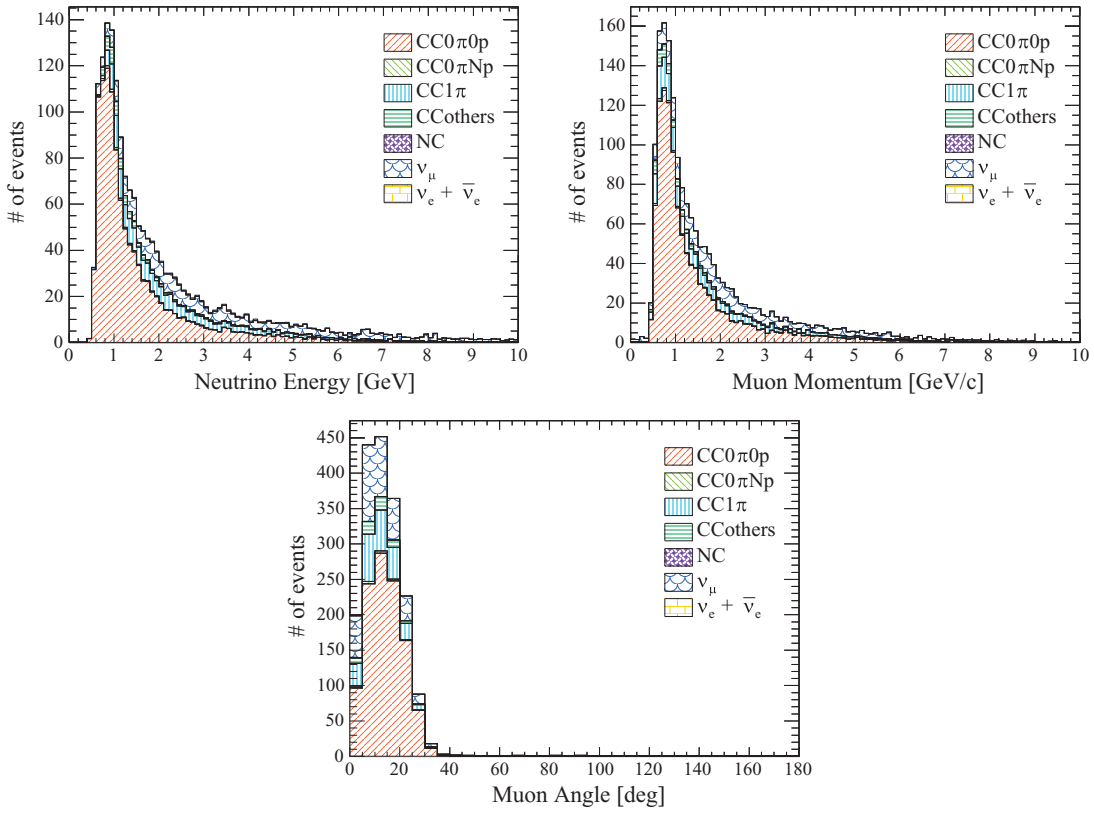

Fig. 11. Simulated true distribution of the selected events in the Proton Module as a function of neutrino energy (top left), muon momentum (top right), and muon angle (bottom).

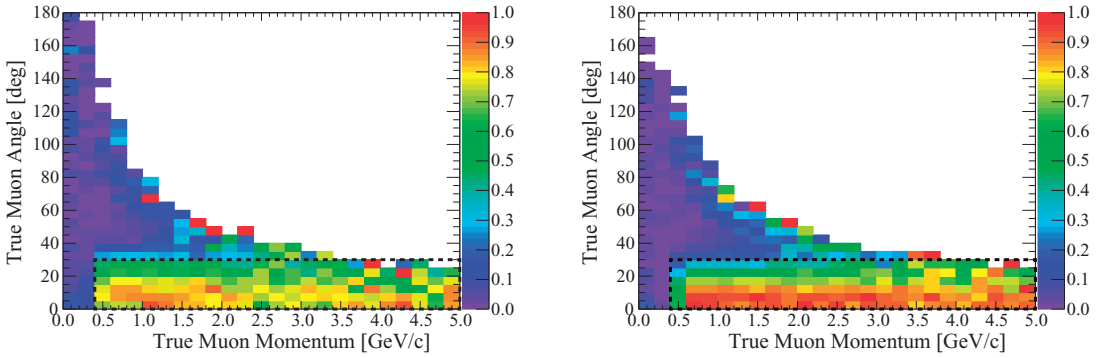

Fig. 12. Detection efficiencies of the WAGASCI module (left) and the Proton Module (right) for $\overline{\nu}_\mu$ CC events with respect to true muon angle and momentum. The z-axis of the plot indicates the detection efficiency. The restricted phase space corresponds to the region inside the dotted square.

Table 4. Bin definition based on true phase space and reconstructed tracks.

Bin number	Muon angle range	True phase space	Reconstructed track
0	0–180°	CCother	Multi-track
1	0–5°	CC0π0p	Single-track
2	5–10°	CC0π0p	Single-track
3	10–15°	CC0π0p	Single-track
4	15–20°	CC0π0p	Single-track
5	20–25°	CC0π0p	Single-track
6	25–30°	CC0π0p	Single-track
7	30–180°	CC0π0p	Single-track

Table 5. Calculated detection efficiencies of $\overline{\nu}_\mu$ and $\overline{\nu}_\mu + \nu_\mu$ CC events for each of the phase-space bins.

	$\overline{\nu}_\mu$		$\overline{\nu}_\mu + \nu_\mu$	
True phase space	WAGASCI	Proton Module	WAGASCI	Proton Module
CCother	0.194	0.237	0.233	0.289
CC0π0p : 0–5°	0.683	0.897	0.682	0.897
CC0π0p : 5–10°	0.738	0.896	0.729	0.892
CC0π0p : 10–15°	0.737	0.830	0.724	0.825
CC0π0p : 15–20°	0.679	0.694	0.674	0.693
CC0π0p : 20–25°	0.552	0.502	0.543	0.507
CC0π0p : 25–30°	0.391	0.305	0.387	0.302
CC0π0p : 30–180°	0.081	0.048	0.081	0.048
Total	0.372	0.397	0.355	0.395

the laboratory frame. According to this restriction, the charged-current events are classified into six bins based on the muon angles, as summarized in Table 4. Although the signal is CC0π0p with a muon angle smaller than 30 degrees, the selected events for cross-section calculations also include two bins for multi-track samples (labeled as CCother) and higher-angle samples (labeled as single track 30–180° CC0π0p). In addition, detectable phase spaces of pions and protons are defined as $\theta_\pi < 70°$, $p_\pi > 200$ MeV/c and $\theta_\mathrm{p} < 70°$, $p_\mathrm{p} > 600$ MeV/c, respectively, in the laboratory frame, and the signal phase space is defined allowing neither pions nor protons in these regions. The detection efficiencies for each bin are summarized in Table 5.

Table 6. Summary of integrated neutrino fluxes and the number of target nucleons used for cross-section calculation. The fluxes are normalized to the actual recorded POT (7.91×10^{20}).

Cross-section	$\Phi_{\bar{\nu}_\mu}$	Φ_{ν_μ}	T_{H_2O}	T_{CH}
σ_{H_2O}	$1.69 \times 10^{13}\,\mathrm{cm}^{-2}$	$1.48 \times 10^{12}\,\mathrm{cm}^{-2}$	4.957×10^{28}	1.107×10^{28}
σ_{CH}	$1.70 \times 10^{13}\,\mathrm{cm}^{-2}$	$1.49 \times 10^{12}\,\mathrm{cm}^{-2}$	–	9.210×10^{28}

5. Cross-section extraction

In this paper, the following notations are used:

- X_j^{reco} represents the jth reconstructed single-track angle bin.
- C_i^{true} represents the ith true angle of muons, pions, and protons.
- A smearing matrix, $\mathbb{P}(X_j^{\mathrm{reco}}|C_i^{\mathrm{true}})$, represents a probability that an event from C_i^{true} is reconstructed in X_j^{reco}.
- An unfolding matrix, $U_{ij} = \mathbb{P}(C_i^{\mathrm{true}}|X_j^{\mathrm{reco}})$, represents a probability that an event in X_j^{reco} derives from an event in C_i^{true}.

The analysis method is almost the same as that used in Ref. [5], and detailed information can be found in that reference.

5.1. *Calculation formula*

The CC0π0p flux-integrated differential cross-sections are calculated as follows:

$$\sigma_{i\ \mathrm{H_2O}} = \sum_j \frac{U_{ij\ \mathrm{WM}}(N_{j\ \mathrm{WM}}^{\mathrm{sel}} - N_{j\ \mathrm{WM}}^{\mathrm{BG}})}{\Phi_{\mathrm{WM}}^{\mathrm{H_2O}} T_{\mathrm{WM}}^{\mathrm{H_2O}} \varepsilon_{i\ \mathrm{WM}}^{\mathrm{H_2O}}} \tag{1}$$

$$\sigma_{i\ \mathrm{CH}} = \sum_j \frac{U_{ij\ \mathrm{PM}}(N_{j\ \mathrm{PM}}^{\mathrm{sel}} - N_{j\ \mathrm{PM}}^{\mathrm{BG}})}{\Phi_{\mathrm{PM}}^{\mathrm{CH}} T_{\mathrm{PM}}^{\mathrm{CH}} \varepsilon_{i\ \mathrm{PM}}^{\mathrm{CH}}} \tag{2}$$

where N^{sel} is the number of selected events, Φ is the integrated $\bar{\nu}_\mu$ ($\bar{\nu}_\mu + \nu_\mu$) flux, T is the number of target nucleons, and ε is the signal-selection efficiency. N^{BG} is the number of expected backgrounds, and $N_{\mathrm{WM}}^{\mathrm{BG}}$ is estimated not only by the MC simulation but also by the calculated cross-section on the hydrocarbon target to take into account the contribution from the plastic scintillators in the WAGASCI module. Quantities Φ and T are summarized in Table 6. U_{ij} is an unfolding matrix that is iteratively calculated based on the D'Agostini method [31]. To avoid any dependence of U_{ij} on the input neutrino-interaction simulation the number of iterations is not truncated but rather run through to convergence such that the result is effectively unregularized (more details are presented in Sect. 7). In the unfolding procedure, we choose a flat prior and define the number of iterations as 1500. The subscripts of WM and PM represent the WAGASCI module and the Proton Module, respectively, and those of H_2O and CH represent target materials.

All of the backgrounds are estimated by the MC simulation, except for interactions on WAGASCI plastic scintillators. They constitute one of the main background sources for σ_{H_2O}, since about 20% of the fiducial volume of the WAGASCI module is occupied by plastic scintillators. They are calculated by normalizing from the number of selected events in the Proton Module.

Table 7. Summary of differences between the $\overline{\nu}_\mu$ and $\overline{\nu}_\mu + \nu_\mu$ cross-section measurements.

	$\overline{\nu}_\mu$ cross-section	$\overline{\nu}_\mu + \nu_\mu$ cross-section
ν_μ CC interaction	Background	Signal
Detection efficiency (ε) Unfolding matrix (U_{ij})	Calculated with $\overline{\nu}_\mu$ samples	Calculated with $\overline{\nu}_\mu + \nu_\mu$ samples
Integrated flux	$\Phi_{\overline{\nu}_\mu}$	$\Phi_{\overline{\nu}_\mu+\nu_\mu}$

5.2. $\overline{\nu}_\mu$ cross-sections and $\overline{\nu}_\mu + \nu_\mu$ cross-sections

As shown in Tables 2 and 3, the ν_μ CC interactions are the dominant background and are irreducible in our $\overline{\nu}_\mu$ event selection since we cannot determine the charge of the outgoing muon. In order to be less model-dependent, we also measured a combined $\overline{\nu}_\mu + \nu_\mu$ cross-section, since this measurement does not rely on model assumptions to subtract the ν_μ background.

The event selection, the number of selected events (N_j^{sel}), and the number of target nucleons (T) are common to the $\overline{\nu}_\mu$ and $\overline{\nu}_\mu + \nu_\mu$ cross-section measurements. Differences between these measurements are summarized in Table 7.

6. Uncertainties

Evaluation methods for each uncertainty are almost the same as those considered in Ref. [5], and detailed information can be found in that reference.

6.1. Systematic uncertainties from neutrino-flux uncertainties

The uncertainty on the neutrino flux is estimated according to knowledge of hadron interactions and the J-PARC beamline. For systematic uncertainties on the cross-section extraction, effects on the number of background events (N^{BG}), integrated flux (Φ), detection efficiency (ε), and the unfolding matrix (U_{ij}) are considered. Events generated in the MC simulation are varied based on the estimated flux uncertainties in bins of the true neutrino energies and correlations between them. The variation of the cross-section is calculated by using 10 000 toy samples accordingly. The $\pm 1\sigma$ range of the distribution is taken as the systematic uncertainty.

The uncertainties from neutrino flux on the integrated cross-section for CC0π0p with a muon angle smaller than 30 degrees are expected to be about 10% for $\sigma_{\mathrm{H_2O}}$ and σ_{CH}, and they give the dominant contributions to the total uncertainty. On the other hand, the uncertainties for the cross-section ratio ($\sigma_{\mathrm{H_2O}}/\sigma_{\mathrm{CH}}$) are about 0.5%, since most of the parameters are strongly correlated and the uncertainties cancel.

6.2. Systematic uncertainties from the neutrino-interaction model

Uncertainties on the neutrino-interaction model are estimated based on the understanding of the model applied to the MC-event generator. Each parameter related to this analysis is varied to cover model uncertainties, and the propagation to the extracted cross-sections is calculated. The parameters with their default values and 1σ variations are summarized in Table 8. When the uncertainty is calculated, no correlation is assumed between different target nuclei for the Fermi momentum (P_{f}), binding energy (E_{b}), 2p2h, CC coherent parameters, and nucleon final-state interactions (FSI). Full correlation between the different targets is assumed for the other parameters.

Table 8. Summary of the default values of the parameters used in the neutrino-interaction model and their uncertainties.

Parameter	Nominal value	Uncertainties (1σ)
CCQE: the Smith–Moniz model RFG with the RPA correction		
$M_{\mathrm{A}}^{\mathrm{QE}}$	1.15 GeV	0.18 GeV
P_{f} ^{12}C	223 MeV	31 MeV
P_{f} ^{16}O	225 MeV	31 MeV
E_{b} ^{12}C	25 MeV	9 MeV
E_{b} ^{16}O	27 MeV	9 MeV
2p2h: the Nieves model		
2p2h normalization ^{12}C	100%	100%
2p2h normalization ^{16}O	100%	100%
2p2h shape ^{12}C	100%	100%
2p2h shape ^{16}O	100%	100%
CC-resonant model: the Rein–Sehgal model		
$M_{\mathrm{A}}^{\mathrm{Res}}$	0.95 GeV	0.15 GeV
C_{A5}	1.01	0.12
Isospin $\frac{1}{2}$ background	1.30	0.20
CC coherent model: the Berger–Sehgal model		
CCcoh normalization ^{12}C	100%	100%
CCcoh normalization ^{16}O	100%	100%
DIS: GRV98 PDF with Bodek–Yang modifications		
DIS correction factor	$x = 0$	$x = 0.40$
NC interactions		
NCcoh norm	100%	30%
NCother norm	100%	30%
Final-state interactions of pions		
Pion absorption normalization	1.1	50%
Pion charge exchange (low-E) normalization	1.0	50%
Pion charge exchange (high-E) normalization	1.8	30%
Pion quasi-elastic (low-E) normalization	1.0	50%
Pion quasi-elastic (high-E) normalization	1.8	30%
Pion inelastic normalization	1.0	50%
Final-state interactions of nucleons		
Nucleon FSI	100%	100%

The uncertainties due to the neutrino-interaction model are dominated by effects from CCQE and 2p2h interactions and nucleon FSI, followed by pion production ($M_{\mathrm{A}}^{\mathrm{Res}}$ and C_{A5}) and Fermi momentum (P_{f}). The CCQE and 2p2h interactions have uncertainties that are 2% larger than other categories and have the largest effect on the detection-efficiency estimation, since they dominate the CC0π0p signal and then largely distort the prior distribution. Nucleon FSIs mainly affect the number of backgrounds via ν_μ interactions, since more nucleons often exist in the final state of ν_μ interactions than that of $\overline{\nu}_\mu$ interactions. Hence, this effect becomes smaller for the $\overline{\nu}_\mu + \nu_\mu$ cross-section measurement.

6.3. Systematic uncertainties from the detector response

Uncertainties on the detector response are estimated based on measurements during the detector construction, commissioning data taking with cosmic muons, and operation with the anti-neutrino beam. Effects on the number of selected events are estimated according to the uncertainty on the detector response, and the systematic uncertainty on the cross-section measurement is estimated by applying fluctuations to the measured number of selected events. In order to apply fluctuations to the number of selected events, no correlation between the WAGASCI module and the Proton Module is assumed, except for the beam-related backgrounds, which should be common between the two detectors. Correlations between each bin of reconstructed tracks are considered. The target mass, MPPC noise, scintillator crosstalk, reconstruction efficiency, event pileup, and beam-related backgrounds are considered as sources of uncertainty. They are estimated by varying the parameters in the MC simulation and calculating the variation in the number of selected events. In addition, uncertainties on the event selection are also taken into account. They are estimated by varying the event selection criteria and calculating the difference between data and simulation in the number of selected events.

6.4. Total uncertainty

Total uncertainties are summarized in Appendix A. For the cross-section measurements of CC0π0p with a muon angle smaller than 30 degrees, the total uncertainty on the absolute cross-sections, σ_{H_2O} and σ_{CH}, is dominated by the neutrino-flux uncertainty, while that on the cross-section ratio, $\sigma_{H_2O}/\sigma_{CH}$, is dominated by statistical errors and errors on the detector response.

7. Results

Figure 13 shows the convergence of extracted cross-sections with respect to the number of iterations. Each cross-section converges to a constant value after 1500 iterations.

The measured flux-integrated CC0π0p cross-sections on H_2O and CH with a muon angle smaller than 30 degrees are summarized as follows:

$$
\begin{aligned}
\sigma^{\overline{\nu}_\mu}_{H_2O} &= \left[1.082 \pm 0.068(\text{stat.})^{+0.145}_{-0.128}(\text{syst.})\right] \times 10^{-39}\text{cm}^2/\text{nucleon},\\
\sigma^{\overline{\nu}_\mu}_{CH} &= \left[1.096 \pm 0.054(\text{stat.})^{+0.132}_{-0.117}(\text{syst.})\right] \times 10^{-39}\text{cm}^2/\text{nucleon},\\
\sigma^{\overline{\nu}_\mu}_{H_2O}/\sigma^{\overline{\nu}_\mu}_{CH} &= 0.987 \pm 0.078(\text{stat.})^{+0.093}_{-0.090}(\text{syst.}),\\
\sigma^{\overline{\nu}_\mu+\nu_\mu}_{H_2O} &= \left[1.155 \pm 0.064(\text{stat.})^{+0.148}_{-0.129}(\text{syst.})\right] \times 10^{-39}\text{cm}^2/\text{nucleon},\\
\sigma^{\overline{\nu}_\mu+\nu_\mu}_{CH} &= \left[1.159 \pm 0.049(\text{stat.})^{+0.129}_{-0.115}(\text{syst.})\right] \times 10^{-39}\text{cm}^2/\text{nucleon},\\
\sigma^{\overline{\nu}_\mu+\nu_\mu}_{H_2O}/\sigma^{\overline{\nu}_\mu+\nu_\mu}_{CH} &= 0.996 \pm 0.069(\text{stat.})^{+0.083}_{-0.078}(\text{syst.}),
\end{aligned}
$$

where the cross-sections are normalized by the number of all nucleons in molecules of H_2O and CH. All the integrated cross-sections are consistent with the models in the MC-event generator, NEUT, within a level of 1σ. Figure 14 shows correlation matrices including all uncertainties for $\overline{\nu}_\mu$ (top) and $\overline{\nu}_\mu + \nu_\mu$ (bottom) cross-sections. Figure 15 shows the distributions of the measured differential cross-sections for CC0π0p with a muon angle smaller than 30 degrees, with their uncertainties and expectations from NEUT (5.3.3). Basically, the measured cross-sections on each phase-space

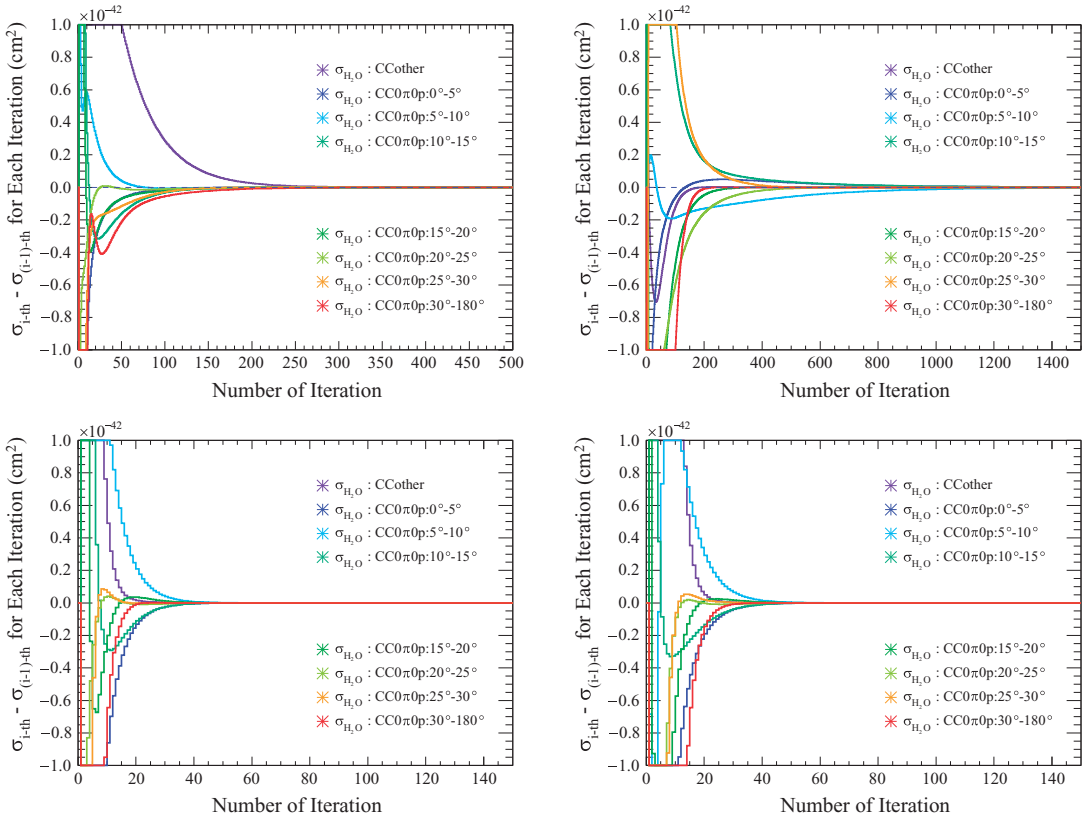

Fig. 13. Convergence of the extracted cross-sections, $\overline{\nu}_\mu$ cross-section (left) and $\overline{\nu}_\mu + \nu_\mu$ cross-section (right). Top line: $\sigma_{\mathrm{H_2O}}$. Bottom line: σ_{CH}. The plots show the first 500 iterations for $\overline{\nu}_\mu$ $\sigma_{\mathrm{H_2O}}$, 150 iterations for $\overline{\nu}_\mu$ σ_{CH}, 1500 iterations for $\overline{\nu}_\mu + \nu_\mu$ $\sigma_{\mathrm{H_2O}}$, 150 iterations for $\overline{\nu}_\mu + \nu_\mu$ σ_{CH}.

bin agree with the NEUT expectation within 1σ, except for $\sigma_{\mathrm{H_2O}}^{\overline{\nu}_\mu+\nu_\mu}$ and $\sigma_{\mathrm{H_2O}}^{\overline{\nu}_\mu+\nu_\mu}/\sigma_{\mathrm{CH}}^{\overline{\nu}_\mu+\nu_\mu}$ in the phase-space region of 20–25°.

In order to evaluate the agreement of measured differential cross-sections with predictions, χ^2 values are calculated based on the total uncertainty including both the statistical and systematic uncertainties. Tables 9 and 10 show the calculated χ^2 values for the predictions from NEUT and GENIE. Considering that the number of degrees of freedom is eight, the calculated χ^2 values suggest that the measured cross-sections agree well with the neutrino-interaction models implemented in those generators.

8. Conclusion

In this paper, we report measurements of (anti-)neutrino cross-sections on water and hydrocarbon targets with the WAGASCI module and the Proton Module using the T2K anti-neutrino beam. The mean neutrino energy is 0.86 GeV and the peak is at 0.66 GeV with a 1σ spread of $^{+0.40}_{-0.25}$ GeV. The signal is taken to be charged-current interactions with one muon and neither pions nor protons produced, based on the kinematic measurements of muons, pions, and protons. The differential cross-sections and integrated cross-sections for the $\overline{\nu}_\mu$ only and $\overline{\nu}_\mu + \nu_\mu$ fluxes are measured. The results agree with the current neutrino-interaction models used in the T2K oscillation analysis within their statistical and systematic uncertainties.

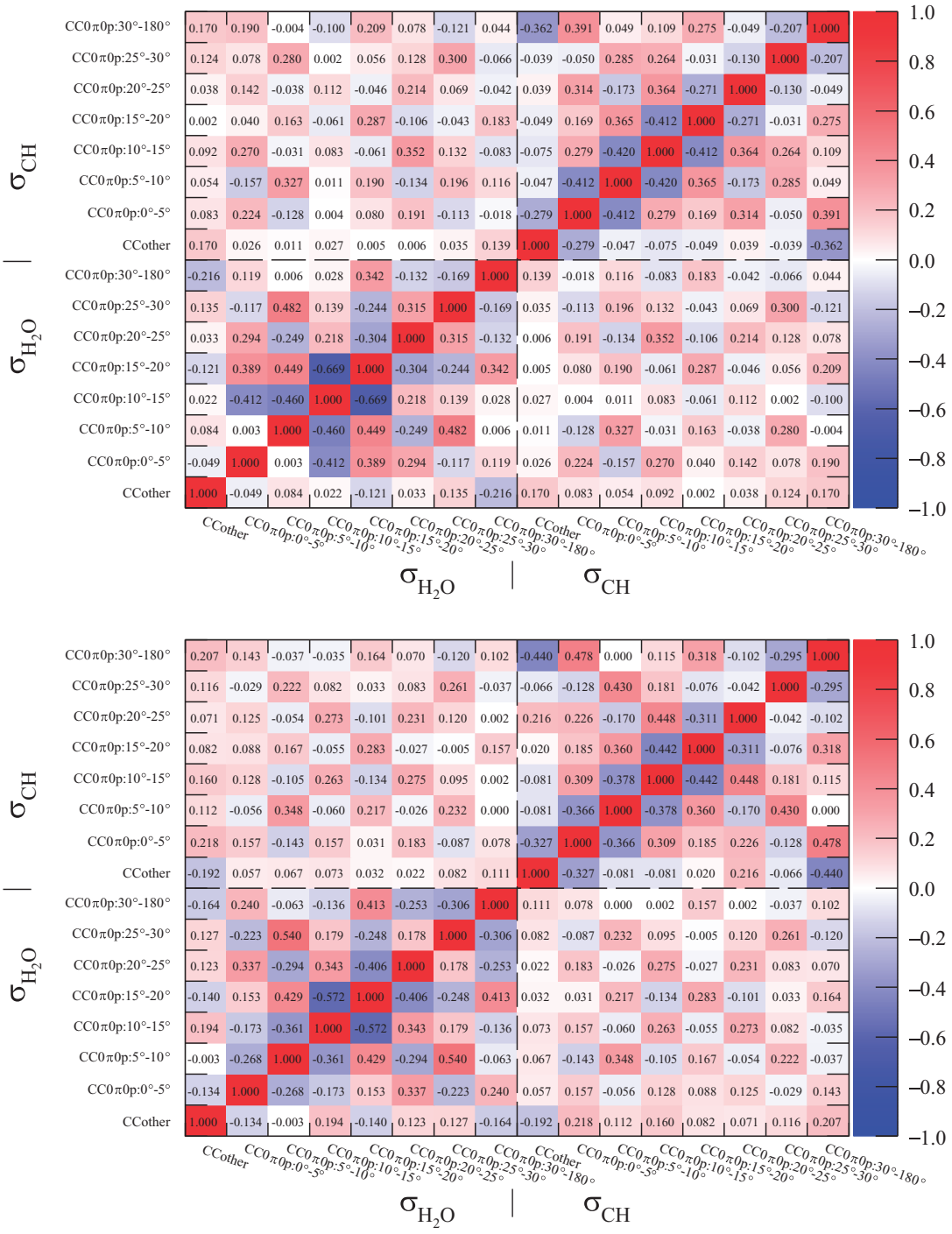

Fig. 14. Correlation matrices including all uncertainties for $\overline{\nu}_\mu$ (top) and $\overline{\nu}_\mu + \nu_\mu$ (bottom) cross-sections.

Acknowledgements

We thank the J-PARC staff for superb accelerator performance. We thank the CERN NA61/SHINE Collaboration for providing valuable particle production data. We acknowledge the support of MEXT, JSPS KAKENHI (JP16H06288, JP18K03682, JP18H03701, JP18H05537, JP19J01119, JP19J22440, JP19J22258, JP20H00162, JP20H00149, JP20J20304) and bilateral programs(JPJSBP120204806, JPJSBP120209601), Japan; NSERC, the NRC, and CFI, Canada; the CEA and CNRS/IN2P3, France; the DFG (RO 3625/2), Germany; the INFN, Italy; the Ministry of Education and Science(DIR/WK/2017/05) and the National Science

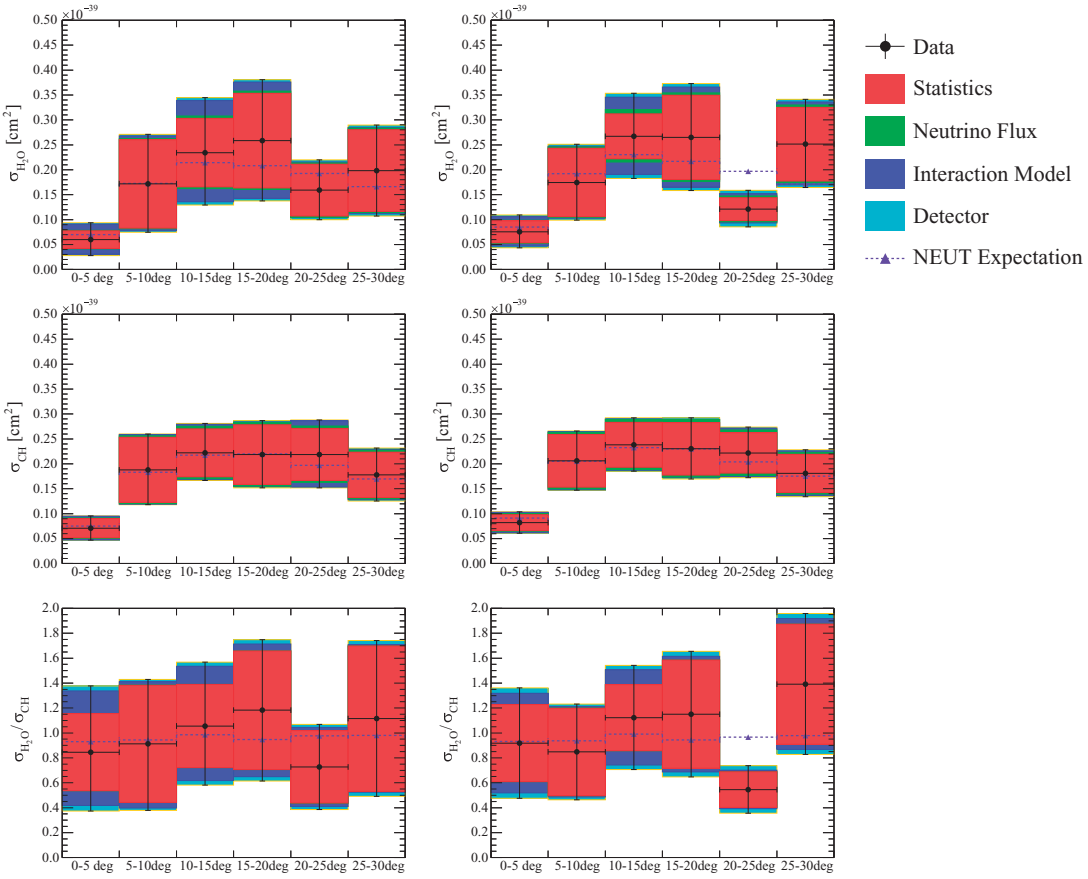

Fig. 15. Measured values for the differential $\overline{\nu}_\mu$ cross-section (left) and $\overline{\nu}_\mu + \nu_\mu$ cross-section (right). Top line: σ_{H_2O}. Middle line: σ_{CH}. Bottom line: $\sigma_{H_2O}/\sigma_{CH}$. Each plot shows the cumulative quadratic sum of the uncertainties from statistics, neutrino flux, neutrino-interaction model, and detector response.

Table 9. Absolute χ^2 values for the $\overline{\nu}_\mu$ and $\overline{\nu}_\mu + \nu_\mu$ cross-sections, with respect to the total uncertainty.

	$\overline{\nu}_\mu$ cross-section			$\overline{\nu}_\mu + \nu_\mu$ cross-section		
	σ_{H_2O}	σ_{CH}	$\sigma_{H_2O}/\sigma_{CH}$	σ_{H_2O}	σ_{CH}	$\sigma_{H_2O}/\sigma_{CH}$
NEUT	3.19	11.34	1.71	7.06	2.63	6.87
GENIE	4.25	14.26	1.83	7.09	3.38	7.55

Table 10. Absolute χ^2 values for the $\overline{\nu}_\mu$ and $\overline{\nu}_\mu + \nu_\mu$ cross-sections only for a muon angle less than 30 degrees, concerning the total uncertainty.

	$\overline{\nu}_\mu$ cross-section			$\overline{\nu}_\mu + \nu_\mu$ cross-section		
	σ_{H_2O}	σ_{CH}	$\sigma_{H_2O}/\sigma_{CH}$	σ_{H_2O}	σ_{CH}	$\sigma_{H_2O}/\sigma_{CH}$
NEUT	0.74	0.16	0.81	5.93	0.33	5.76
GENIE	0.72	0.54	0.89	5.98	0.57	6.35

Centre (UMO-2018/30/E/ST2/00441), Poland; the RSF (19-12-00325), RFBR(JSPS-RFBR 20-52-50010\20) and the Ministry of Science and Higher Education(075-15-2020-778), Russia; MICINN (SEV-2016-0588, PID2019-107564GB-I00, PGC2018-099388-BI00) and ERDF funds and CERCA program, Spain; the SNSF and SERI (200021_185012, 200020_188533, 20FL21_186178I), Switzerland; the STFC, UK; and the DOE,

USA. We also thank CERN for the UA1/NOMAD magnet, DESY for the HERA-B magnet mover system, NII for SINET5, the WestGrid and SciNet consortia in Compute Canada, and GridPP in the United Kingdom. In addition, the participation of individual researchers and institutions has been further supported by funds from the ERC (FP7), "la Caixa" Foundation (ID 100010434, fellowship code LCF/BQ/IN17/11620050), the European Union's Horizon 2020 Research and Innovation Programme under the Marie Sklodowska-Curie grant agreement numbers 713673 and 754496, and H2020 grant numbers RISE-GA822070-JENNIFER2 2020 and RISE-GA872549-SK2HK; the JSPS, Japan; the Royal Society, UK; French ANR grant number ANR-19-CE31-0001; and the DOE Early Career programme, USA.

Funding

Open Access funding: SCOAP[3].

Appendix A. Differential cross-sections

The $\overline{\nu}_\mu$ and $\overline{\nu}_\mu + \nu_\mu$ cross-section measurements are summarized in Tables A.1 and A.2. Total uncertainties are summarized in Tables A.3 and A.4. The total uncertainty in the right-hand column is calculated as a quadratic sum of the statistical uncertainty and the systematic uncertainties. The fractional uncertainties are shown in Fig. A.1. By taking the water-to-hydrocarbon cross-section ratio, uncertainties on the T2K (anti-)neutrino beam prediction, which are the dominant errors for absolute cross-section measurements, largely cancel.

Table A.1. Summary of the $\overline{\nu}_\mu$ cross-section measurement. Units for σ_{H_2O} and σ_{CH} are [$\times 10^{-39}$ cm^2/nucleon].

	True phase space	Cross-section	Stat. err.	Syst. err.
σ_{H_2O}	CCother	0.244	$\pm$0.120	$+0.206/-0.199$
	CC0π0p : 0–5°	0.060	$\pm$0.018	$+0.029/-0.027$
	CC0π0p : 5–10°	0.172	$\pm$0.089	$+0.045/-0.040$
	CC0π0p : 10–15°	0.234	$\pm$0.069	$+0.086/-0.080$
	CC0π0p : 15–20°	0.259	$\pm$0.095	$+0.077/-0.075$
	CC0π0p : 20–25°	0.159	$\pm$0.052	$+0.031/-0.029$
	CC0π0p : 25–30°	0.198	$\pm$0.082	$+0.040/-0.039$
	CC0π0p : 30–180°	0.635	$\pm$0.145	$+0.243/-0.217$
	CCTotal	1.961	$\pm$0.196	$+0.400/-0.368$
	CC0π0p : 0–30°	1.082	$\pm$0.068	$+0.145/-0.128$
σ_{CH}	CCother	0.162	$\pm$0.057	$+0.149/-0.141$
	CC0π0p : 0–5°	0.071	$\pm$0.019	$+0.015/-0.014$
	CC0π0p : 5–10°	0.188	$\pm$0.065	$+0.029/-0.025$
	CC0π0p : 10–15°	0.222	$\pm$0.048	$+0.034/-0.028$
	CC0π0p : 15–20°	0.219	$\pm$0.060	$+0.033/-0.030$
	CC0π0p : 20–25°	0.219	$\pm$0.052	$+0.045/-0.042$
	CC0π0p : 25–30°	0.178	$\pm$0.046	$+0.028/-0.025$
	CC0π0p : 30–180°	0.975	$\pm$0.285	$+0.320/-0.344$
	CCTotal	2.233	$\pm$0.195	$+0.498/-0.446$
	CC0π0p : 0–30°	1.096	$\pm$0.054	$+0.132/-0.117$
$\sigma_{H_2O}/\sigma_{CH}$	CCother	1.508	$\pm$0.753	$+1.803/-1.524$
	CC0π0p : 0–5°	0.846	$\pm$0.310	$+0.431/-0.356$
	CC0π0p : 5–10°	0.913	$\pm$0.470	$+0.213/-0.253$
	CC0π0p : 10–15°	1.056	$\pm$0.334	$+0.389/-0.336$
	CC0π0p : 15–20°	1.183	$\pm$0.476	$+0.306/-0.312$
	CC0π0p : 20–25°	0.728	$\pm$0.291	$+0.176/-0.179$
	CC0π0p : 25–30°	1.115	$\pm$0.583	$+0.227/-0.219$
	CC0π0p : 30–180°	0.651	$\pm$0.241	$+0.291/-0.299$
	CCTotal	0.878	$\pm$0.111	$+0.177/-0.191$
	CC0π0p : 0–30°	0.987	$\pm$0.078	$+0.093/-0.090$

Table A.2. Summary of the $\overline{\nu}_\mu + \nu_\mu$ cross-section measurement. Units for σ_{H_2O} and σ_{CH} are $[\times 10^{-39}\ \mathrm{cm}^2/\mathrm{nucleon}]$.

	True phase space	Cross-section	Stat. err.	Syst. err.
σ_{H_2O}	CCother	0.923	± 0.126	$+0.224/-0.219$
	CC0π0p : 0–5°	0.075	± 0.022	$+0.026/-0.023$
	CC0π0p : 5–10°	0.175	± 0.069	$+0.034/-0.032$
	CC0π0p : 10–15°	0.267	± 0.045	$+0.074/-0.072$
	CC0π0p : 15–20°	0.265	± 0.085	$+0.067/-0.065$
	CC0π0p : 20–25°	0.121	± 0.023	$+0.030/-0.027$
	CC0π0p : 25–30°	0.252	± 0.074	$+0.051/-0.046$
	CC0π0p : 30–180°	0.590	± 0.185	$+0.235/-0.217$
	CCTotal	2.668	± 0.171	$+0.353/-0.327$
	CC0π0p : 0–30°	1.155	± 0.064	$+0.148/-0.129$
σ_{CH}	CCother	0.877	± 0.062	$+0.364/-0.344$
	CC0π0p : 0–5°	0.082	± 0.016	$+0.015/-0.014$
	CC0π0p : 5–10°	0.206	± 0.053	$+0.028/-0.025$
	CC0π0p : 10–15°	0.238	± 0.045	$+0.030/-0.027$
	CC0π0p : 15–20°	0.230	± 0.053	$+0.033/-0.030$
	CC0π0p : 20–25°	0.222	± 0.040	$+0.032/-0.029$
	CC0π0p : 25–30°	0.181	± 0.038	$+0.028/-0.026$
	CC0π0p : 30–180°	0.969	± 0.228	$+0.280/-0.309$
	CCTotal	3.005	± 0.175	$+0.499/-0.444$
	CC0π0p : 0–30°	1.159	± 0.049	$+0.129/-0.115$
$\sigma_{H_2O}/\sigma_{CH}$	CCother	1.052	± 0.169	$+0.563/-0.519$
	CC0π0p : 0–5°	0.919	± 0.310	$+0.318/-0.316$
	CC0π0p : 5–10°	0.848	± 0.352	$+0.152/-0.156$
	CC0π0p : 10–15°	1.123	± 0.265	$+0.325/-0.321$
	CC0π0p : 15–20°	1.151	± 0.435	$+0.256/-0.255$
	CC0π0p : 20–25°	0.546	± 0.143	$+0.127/-0.124$
	CC0π0p : 25–30°	1.391	± 0.482	$+0.300/-0.293$
	CC0π0p : 30–180°	0.609	± 0.251	$+0.297/-0.273$
	CCTotal	0.888	± 0.077	$+0.148/-0.160$
	CC0π0p : 0–30°	0.996	± 0.069	$+0.083/-0.078$

Table A.3. Summary of systematic uncertainties on the $\overline{\nu}_\mu$ cross-section [%].

	True phase space	Statistics	Neutrino flux	Neutrino interactions	Detector response	Total
σ_{H_2O}	CCother	±49.4	$^{+8.5}_{-7.2}$	$^{+57.3}_{-53.2}$	±61.7	$^{+98.0}_{-95.5}$
	CC0π0p : 0–5°	±29.5	$^{+10.7}_{-9.0}$	$^{+41.2}_{-37.7}$	±22.2	$^{+56.4}_{-53.5}$
	CC0π0p : 5–10°	±51.6	$^{+11.4}_{-9.5}$	$^{+19.4}_{-16.1}$	±13.9	$^{+58.0}_{-56.6}$
	CC0π0p : 10–15°	±29.3	$^{+11.0}_{-9.3}$	$^{+31.6}_{-28.8}$	±15.3	$^{+47.1}_{-44.9}$
	CC0π0p : 15–20°	±36.7	$^{+10.9}_{-9.3}$	$^{+24.3}_{-24.0}$	±13.3	$^{+47.3}_{-46.7}$
	CC0π0p : 20–25°	±32.7	$^{+10.6}_{-9.1}$	$^{+8.3}_{-6.8}$	±14.2	$^{+38.1}_{-37.4}$
	CC0π0p : 25–30°	±41.5	$^{+11.1}_{-9.4}$	$^{+8.2}_{-8.9}$	±14.9	$^{+46.2}_{-45.9}$
	CC0π0p : 30–180°	±22.8	$^{+10.3}_{-8.7}$	$^{+29.4}_{-24.5}$	±22.2	$^{+44.5}_{-41.1}$
	CCTotal	±10.0	$^{+9.6}_{-8.2}$	$^{+15.7}_{-14.3}$	±9.0	$^{+22.7}_{-21.3}$
	CC0π0p : 0–30°	±6.3	$^{+10.9}_{-9.2}$	$^{+5.6}_{-5.0}$	±5.5	$^{+14.8}_{-13.4}$
σ_{CH}	CCother	±35.5	$^{+8.6}_{-7.4}$	$^{+81.8}_{-76.1}$	±41.2	$^{+98.6}_{-93.8}$
	CC0π0p : 0–5°	±27.1	$^{+10.8}_{-9.2}$	$^{+17.3}_{-16.4}$	±7.4	$^{+34.8}_{-33.9}$
	CC0π0p : 5–10°	±34.8	$^{+10.8}_{-9.1}$	$^{+9.6}_{-7.8}$	±5.8	$^{+38.1}_{-37.2}$
	CC0π0p : 10–15°	±21.7	$^{+10.4}_{-9.0}$	$^{+9.3}_{-5.9}$	±6.6	$^{+26.6}_{-25.1}$
	CC0π0p : 15–20°	±27.4	$^{+10.8}_{-9.2}$	$^{+4.8}_{-4.4}$	±9.0	$^{+31.2}_{-30.6}$
	CC0π0p : 20–25°	±23.8	$^{+10.8}_{-9.2}$	$^{+16.2}_{-15.2}$	±7.1	$^{+31.6}_{-30.6}$
	CC0π0p : 25–30°	±25.7	$^{+10.4}_{-8.8}$	$^{+7.9}_{-6.8}$	±9.0	$^{+30.2}_{-29.4}$
	CC0π0p : 30–180°	±29.3	$^{+10.4}_{-9.0}$	$^{+29.1}_{-32.2}$	±11.1	$^{+44.0}_{-45.8}$
	CCTotal	±8.8	$^{+9.6}_{-8.1}$	$^{+19.5}_{-17.5}$	±5.3	$^{+24.0}_{-21.8}$
	CC0π0p : 0–30°	±5.0	$^{+10.6}_{-9.1}$	$^{+4.5}_{-4.3}$	±3.8	$^{+13.0}_{-11.8}$
$\sigma_{H_2O}/\sigma_{CH}$	CCother	±49.9	$^{+0.6}_{-0.6}$	$^{+107.8}_{-86.9}$	±51.7	$^{+129.6}_{-112.7}$
	CC0π0p : 0–5°	±36.6	$^{+1.7}_{-1.6}$	$^{+45.2}_{-34.8}$	±23.6	$^{+62.8}_{-55.8}$
	CC0π0p : 5–10°	±51.5	$^{+1.5}_{-1.5}$	$^{+17.5}_{-23.0}$	±15.4	$^{+56.6}_{-58.5}$
	CC0π0p : 10–15°	±31.6	$^{+1.1}_{-1.1}$	$^{+32.6}_{-26.8}$	±17.1	$^{+48.5}_{-44.9}$
	CC0π0p : 15–20°	±40.3	$^{+0.8}_{-0.8}$	$^{+19.7}_{-20.3}$	±16.8	$^{+47.9}_{-48.1}$
	CC0π0p : 20–25°	±40.0	$^{+0.9}_{-0.9}$	$^{+17.2}_{-17.7}$	±17.0	$^{+46.8}_{-46.9}$
	CC0π0p : 25–30°	±52.3	$^{+1.6}_{-1.6}$	$^{+10.0}_{-8.5}$	±17.6	$^{+56.1}_{-55.9}$
	CC0π0p : 30–180°	±37.0	$^{+1.4}_{-1.4}$	$^{+36.4}_{-37.9}$	±26.0	$^{+58.0}_{-59.0}$
	CCTotal	±12.6	$^{+0.4}_{-0.4}$	$^{+17.1}_{-19.0}$	±10.6	$^{+23.8}_{-25.1}$
	CC0π0p : 0–30°	±7.9	$^{+0.5}_{-0.5}$	$^{+6.2}_{-5.8}$	±7.0	$^{+12.3}_{-12.1}$

Table A.4. Summary of systematic uncertainties on the $\overline{\nu}_\mu + \nu_\mu$ cross-section [%].

	True phase space	Statistics	Neutrino flux	Neutrino interactions	Detector response	Total
σ_{H_2O}	CCother	±13.6	$^{+8.3}_{-7.0}$	$^{+14.3}_{-14.1}$	±17.8	$^{+27.8}_{-27.4}$
	CC0π0p : 0–5°	±29.3	$^{+10.4}_{-8.9}$	$^{+25.9}_{-21.6}$	±19.2	$^{+44.8}_{-42.1}$
	CC0π0p : 5–10°	±39.4	$^{+11.0}_{-9.2}$	$^{+8.2}_{-7.6}$	±13.8	$^{+44.0}_{-43.4}$
	CC0π0p : 10–15°	±16.8	$^{+10.9}_{-9.4}$	$^{+21.5}_{-21.2}$	±13.4	$^{+32.3}_{-31.6}$
	CC0π0p : 15–20°	±32.0	$^{+10.7}_{-9.1}$	$^{+18.0}_{-17.7}$	±14.1	$^{+40.7}_{-40.2}$
	CC0π0p : 20–25°	±19.1	$^{+10.6}_{-9.1}$	$^{+12.9}_{-8.9}$	±18.2	$^{+31.2}_{-29.3}$
	CC0π0p : 25–30°	±29.4	$^{+10.7}_{-9.2}$	$^{+12.2}_{-10.5}$	±11.9	$^{+35.6}_{-34.7}$
	CC0π0p : 30–180°	±31.3	$^{+10.3}_{-8.7}$	$^{+30.7}_{-27.0}$	±23.3	$^{+50.7}_{-48.3}$
	CCTotal	±6.4	$^{+9.3}_{-8.0}$	$^{+5.8}_{-5.6}$	±7.4	$^{+14.7}_{-13.8}$
	CC0π0p : 0–30°	±5.5	$^{+10.6}_{-9.1}$	$^{+5.0}_{-4.0}$	±5.2	$^{+13.9}_{-12.5}$
σ_{CH}	CCother	±7.1	$^{+8.6}_{-7.3}$	$^{+39.5}_{-37.3}$	±9.6	$^{+42.1}_{-39.9}$
	CC0π0p : 0–5°	±19.4	$^{+10.4}_{-8.8}$	$^{+13.0}_{-12.9}$	±6.4	$^{+26.3}_{-25.7}$
	CC0π0p : 5–10°	±25.7	$^{+10.8}_{-9.2}$	$^{+6.5}_{-6.4}$	±5.1	$^{+29.0}_{-28.5}$
	CC0π0p : 10–15°	±19.0	$^{+10.0}_{-8.6}$	$^{+4.8}_{-4.7}$	±6.1	$^{+22.8}_{-22.2}$
	CC0π0p : 15–20°	±22.8	$^{+10.7}_{-9.2}$	$^{+4.2}_{-4.4}$	±8.4	$^{+26.9}_{-26.4}$
	CC0π0p : 20–25°	±18.2	$^{+10.3}_{-8.9}$	$^{+7.7}_{-6.3}$	±6.9	$^{+23.3}_{-22.3}$
	CC0π0p : 25–30°	±21.2	$^{+9.9}_{-8.5}$	$^{+8.5}_{-8.3}$	±8.4	$^{+26.3}_{-25.7}$
	CC0π0p : 30–180°	±23.5	$^{+10.3}_{-9.0}$	$^{+24.5}_{-28.4}$	±11.3	$^{+37.3}_{-39.6}$
	CCTotal	±5.8	$^{+9.4}_{-7.9}$	$^{+13.2}_{-12.0}$	±3.6	$^{+17.6}_{-15.9}$
	CC0π0p : 0–30°	±4.2	$^{+10.3}_{-8.9}$	$^{+2.7}_{-2.9}$	±3.4	$^{+11.9}_{-10.8}$
$\sigma_{H_2O}/\sigma_{CH}$	CCother	±16.0	$^{+0.6}_{-0.7}$	$^{+49.4}_{-44.6}$	±20.6	$^{+55.9}_{-51.9}$
	CC0π0p : 0–5°	±33.7	$^{+1.6}_{-1.6}$	$^{+27.6}_{-27.3}$	±20.9	$^{+48.3}_{-48.2}$
	CC0π0p : 5–10°	±41.5	$^{+1.6}_{-1.6}$	$^{+9.5}_{-10.3}$	±15.2	$^{+45.2}_{-45.4}$
	CC0π0p : 10–15°	±23.6	$^{+1.7}_{-1.7}$	$^{+24.6}_{-24.2}$	±15.2	$^{+37.4}_{-37.1}$
	CC0π0p : 15–20°	±37.8	$^{+1.5}_{-1.4}$	$^{+13.9}_{-13.9}$	±17.3	$^{+43.8}_{-43.8}$
	CC0π0p : 20–25°	±26.3	$^{+0.9}_{-0.9}$	$^{+11.1}_{-10.1}$	±20.3	$^{+35.1}_{-34.8}$
	CC0π0p : 25–30°	±34.6	$^{+1.7}_{-1.7}$	$^{+15.3}_{-14.6}$	±15.0	$^{+40.8}_{-40.5}$
	CC0π0p : 30–180°	±41.1	$^{+1.9}_{-1.8}$	$^{+40.2}_{-35.3}$	±27.4	$^{+63.8}_{-60.8}$
	CCTotal	±8.7	$^{+0.3}_{-0.3}$	$^{+14.2}_{-15.4}$	±8.6	$^{+18.8}_{-20.0}$
	CC0π0p : 0–30°	±6.9	$^{+0.5}_{-0.6}$	$^{+5.2}_{-4.3}$	±6.5	$^{+10.9}_{-10.5}$

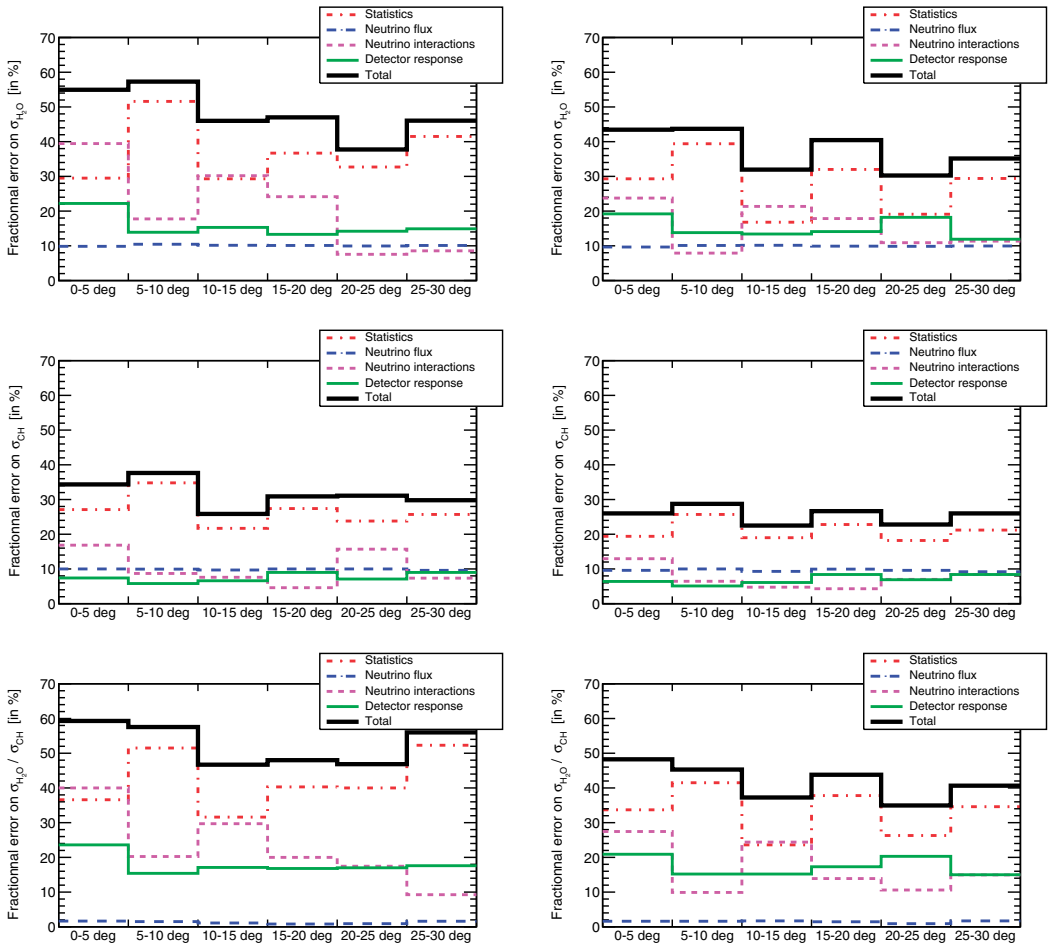

Fig. A.1. Fractional uncertainties on the $\overline{\nu}_\mu$ (left) and $\overline{\nu}_\mu + \nu_\mu$ (right) cross-section measurements.

References

[1] K. Abe et al., Nucl. Instrum. Meth. A **659**, 106 (2011) [arXiv:1106.1238 [physics.ins-det]] [Search INSPIRE].
[2] P.-A. Amaudruz et al., Nucl. Instrum. Meth. A **696**, 1 (2012) [arXiv:1204.3666 [physics.ins-det]] [Search INSPIRE].
[3] K. Abe et al. [T2K Collaboration], Phys. Rev. D **97**, 012001 (2018).
[4] K. Abe et al. [T2K Collaboration], Phys. Rev. D **95**, 012010 (2017).
[5] K. Abe et al. [T2K Collaboration], Prog. Theor. Exp. Phys. **2019**, 093C02 (2019).
[6] K. Abe et al., Phys. Rev. D **102**, 012007 (2020) [arXiv:1908.10249 [hep-ex]] [Search INSPIRE].
[7] K. Kin, Y. Azuma, T. Inoue, Y. Seiya, and K. Yamamoto [J-PARC T59 Collaboration], PoS **NuFact2017**, 155 (2017).
[8] K. Abe et al. [T2K Collaboration], Phys. Rev. D **90**, 052010 (2014).
[9] K. Abe et al., Nucl. Instrum. Meth. A **694**, 211 (2012).
[10] K.K. Hamamatsu Photonics (available at: https://www.hamamatsu.com).
[11] N. Chikuma et al., PoS **EPS-HEP2017**, 780 (2017).
[12] A. Vacheret, S. Greenwood, M. Noy, M. Raymond, and A. Weber, 2007 IEEE Nuclear Science Symp. Conf. Record, Vol. 3, p. 1984 (2007).
[13] K. Abe et al. [T2K Collaboration], Phys. Rev. D **87**, 012001 (2013); **87**, 019902 (2013) [erratum].
[14] Y. Hayato, Acta Phys. Polon. B **40**, 2477 (2009).
[15] S. Agostinelli et al., Nucl. Instrum. Meth. A **506**, 250 (2003).

[16] N. Abgrall et al. [NA61/SHINE Collaboration], Eur. Phys. J. C **76**, 84 (2016) [arXiv:1510.02703 [hep-ex]] [Search INSPIRE].
[17] C. Andreopoulos et al., Nucl. Instrum. Meth. A **614**, 87 (2010).
[18] R. A. Smith and E. J. Moniz, Nucl. Phys. B **43**, 605 (1972); **101**, 547 (1975) [erratum].
[19] A. Bodek and J. L. Ritchie, Phys. Rev. D **23**, 1070 (1981).
[20] A. Bodek and J. L. Ritchie, Phys. Rev. D **24**, 1400 (1981).
[21] J. Nieves, J. E. Amaro, and M. Valverde, Phys. Rev. C **70**, 055503 (2004); **72**, 019902 (2005) [erratum].
[22] J. Nieves, I. Ruiz Simo, and M. J. Vicente Vacas, Phys. Rev. C **83**, 045501 (2011).
[23] D. Rein and L. M. Sehgal, Ann. Phys. **133**, 79 (1981).
[24] D. Rein and L. M. Sehgal, Nucl. Phys. B **223**, 29 (1983).
[25] Ch. Berger and L. M. Sehgal, Phys. Rev. D **79**, 053003 (2009).
[26] M. Glück, E. Reya, and A. Vogt, Eur. Phys. J. C **5**, 461 (1998).
[27] A. Bodek, I. Park, and U. K. Yang, Nucl. Phys. B Proc. Suppl. **139**, 113 (2005).
[28] T. Yang, C. Andreopoulos, H. Gallagher, K. Hofmann, and P. Kehayias, Eur. Phys. J. C **63**, 1 (2009).
[29] K. Abe et al. [T2K Collaboration], Phys. Rev. Lett. **121**, 171802 (2018).
[30] H. Maesaka, Evidence For Muon Neutrino Oscillation In An Accelerator-based Experiment. *Ph.D. Thesis*, Kyoto University (2005).
[31] G. D'Agostini, arXiv:1010.0632 [physics.data-an] [Search INSPIRE].